

# The Gravitomagnetic Field and Penrose Processes

Reva Kay Williams \*

*Department of Astronomy, University of Florida, Gainesville, Florida 32611.*

Results from general relativistic theoretical Monte Carlo computer simulations of Compton scattering and  $e^-e^+$  pair production processes in the ergosphere of a supermassive ( $\sim 10^8 M_\odot$ ) rotating black hole are presented. Particles from an accretion disk fall into the ergosphere and scatter off particles that are in bound equatorial and nonequatorially confined orbits. The Penrose mechanism, in general, allows rotational energy of a Kerr black hole to be extracted by scattered particles escaping from the ergosphere to infinity (i.e., large distances from the black hole). The results of these model calculations show that a form of the Penrose mechanism is capable of producing the observed high energy particles (up to  $\sim$  GeV) emitted by quasars and other active galactic nuclei (AGNs), without the necessity of the external electromagnetic field of the accretion disk. Importantly, these model calculations show that the Lense-Thirring effect, i.e., the dragging of inertial frames into rotation, caused by the angular momentum of the rotating black hole, results in a gravitomagnetic (GM) force being exerted on the scattered escaping particles. Inside the ergosphere, where this dragging is severe, it appears that the GM vector field lines are frame dragged into the positive azimuthal direction, i.e., the direction of rotation of the black hole. The resulting GM force acting on the Penrose scattered particles produces symmetrical and asymmetrical (or one-sided) particle emissions in the polar direction, consistent with the astrophysical jets observed in radio strong AGNs. Note, these Penrose processes can apply to any size rotating black hole.

97.60.Lf, 95.30.Sf, 98.54.-h, 98.54.Cm

## I. INTRODUCTION

In 1918, it was discovered in the equations of general relativity by Thirring and Lense [1] that the angular momentum of a massive body causes inertial frames to be dragged around in the direction that the mass is rotating. In 1969, Roger Penrose [2] noted that, inside the ergosphere of a rotating black hole, this frame dragging is so extreme that it can provide a way to extract rotational energy (we now call this the Penrose mechanism). In this paper, I present the results of the first *complete*, fully general relativistic, four-dimensional, theoretical and numerical model calculation using the Penrose mechanism to extract high energy electrons and photons from a rotating black hole. Penrose scattering processes in the ergosphere allow high energy particles to escape to infinity (far away from the black hole) with a portion of the rotational energy of the Kerr black hole (KBH), and orbital energy-momentum produced by its strong gravitational field. This model calculation not only confirms the results of energy extracted from Penrose Compton scattering processes given in [3,4], however, extracting higher energies when nonequatorially confined targets are introduced, but this model gives space momenta of individual scattered particles, thus, in this sense, making it a complete calculation. Importantly, the Penrose pair production, by photons in bound unstable *trapped* orbits with photons on radially infalling geodesics, at the *photon orbit*, allow electron-positron ( $e^-e^+$ ) pairs to escape with energies as high as  $\sim 4$  GeV (implying a Lorentz factor  $\gamma_e \sim 10^4$ ), or higher depending on properties of the accretion disk. Up until the investigation reported here and the related paper of [5], such Penrose pair production (PPP) at the photon orbit had yet to be proposed. The reason for this is probably because the trajectories for massless and material particles, in nonequatorially confined orbits, i.e., orbits not confined to the equatorial plane of the KBH, had to be solved first to obtain analytical expressions for the conserved energy  $E$  and conserved azimuthal angular momentum  $L$ , as measured by an observer at infinity; this is done in [5], and the results are presented again here in Section II A.

The *classical* Penrose process utilizes the existence of retrograde particle orbits (with respect to the rotation of the KBH) in the ergosphere, for which the energy, as would be measured by an observer at infinity, is negative [2,3]. Such orbits do not come out to infinity. However, it is possible for a particle, say  $p_1$ , that has fallen inwardly from infinity into the ergosphere to scatter off another particle, say  $p_2$ , initially in a direct orbit inside the ergosphere. If the orbit of the scattering particle  $p_2$  changes into a retrograde orbit (of negative energy), then the scattered particle  $p_1$  can escape to infinity with more mass-energy than the sum of the initial energies of  $p_1$  and  $p_2$ . Since the orbit of the initially bound particle  $p_2$  is dependent on the angular momentum of the KBH and the curvature of spacetime

---

\*E-mail: revak@astro.ufl.edu.

defined by the mass of the hole, when  $p_2$  gives up energy to the escaping particle  $p_1$  and falls into the event horizon, the KBH loses energy in the form of rotational energy.

One plausible class of Penrose processes occurs when particles already inside the ergosphere (say particles of an accretion disk) undergo *local relativistic scatterings* [6,7]. Such types are considered in this investigation. If one of the scattering particles is initially in a bound orbit, then it is possible for the other initially unbound scattered particle, or the new particles created in the scattering process, to escape to infinity with rotational energy-momentum from the KBH, extracted either directly (classical Penrose process) or indirectly (quasi-Penrose process), as defined in [5]. This process allows scattered ergospheric particles to (1) escape to infinity with more mass-energy than they would have had if the scattering occurred outside the ergosphere and (2) escape to infinity with mass-energy initially trapped by the KBH, mass-energy near the event horizon that had no other way of escaping, except by such processes as these Penrose processes; otherwise this trapped mass-energy would eventually be accreted into the black hole. That is, since, in general, nothing can come out of the black hole (including for orbits near the event horizon), then a physical process near the hole, such as a Penrose process, is necessary to inject a trapped or “plunging” orbiting particle into an escaping orbit [7]. In other words, these so-called Penrose processes provide away for blueshifted mass-energy, initially trapped by the KBH, to escape to infinity.

The model calculations discussed in this paper consist of using the Monte Carlo method to treat Penrose processes in the ergosphere of a KBH. The processes investigated are Penrose Compton scattering (PCS),  $\gamma$ -ray—proton PPP ( $\gamma p \rightarrow e^- e^+ p$ ), and  $\gamma$ -ray— $\gamma$ -ray PPP ( $\gamma\gamma \rightarrow e^- e^+$ ). These three processes are assumed to occur in material that has fallen into the ergospheric region of a rotating black hole from a surrounding accretion disk. The Monte Carlo method is applied to the cross section of each scattering event to determine values of the scattering angles and final energies as measured by local observers.

In [5], I present the detailed model calculations for the above Penrose scattering processes; the final outcome is the four-momenta of the scattered particles as measured by an observer at infinity. The important properties and relations found from the model calculations of [5] are described in this paper. Now, of the three Penrose scattering processes investigated, the most rewarding ones were the PCS and the PPP ( $\gamma\gamma \rightarrow e^- e^+$ ): these two processes are specifically discussed in this paper. Unfortunately, the PPP ( $\gamma p \rightarrow e^- e^+ p$ ) as suggested in [8,9] did not allow any of the scattered  $e^- e^+$  pairs to escape, mainly because of the large inward radial momentum acquired by the assumed radially infalling incident photon at the scattering radius, too large for the pairs to be scattered outward by the target orbiting proton: I refer the reader to [5] for details concerning this scattering process.

The purpose of this paper is to discuss some of the astrophysically interesting features found by looking carefully at the emission spectra of the Penrose scattered particles. Two of the most important features of the scattered particles are the following: (1) large fluxes of relativistic  $e^- e^+$  pairs with energies as high as  $\gtrsim 4$  GeV can escape; and (2) the rotation of the KBH can cause the scattered particles to escape with asymmetrical distributions, above and below the equatorial plane, thus, naturally aiding in the production of one-sided jets of relativistic particles. Feature (2) is a general relativistic effect caused by the gravitomagnetic field [10] (i.e., the gravitational analog or resemblance of a magnetic field), due to the angular momentum of the rotating black hole. This gravitomagnetic (GM) field, as described in Section IID, causes the dragging of inertial frames, while at the same time produces a force which acts on the momentum vector of a particle in its field, and which, for small velocities ( $\ll c$ ), is linear in the particle’s velocity. Both of the above features are important ingredients in what would be needed to explain the observed spectra of quasars and other AGNs. Note, feature (2) implies that, near the event horizon the expected reflection symmetry of the Kerr metric, above and below the equatorial plane, appears to be broken due to the GM force field.

It has been suggested [11] that the one-sided or asymmetrical jets of radio strong quasars and radio galaxies may be intrinsically related to the energy source. The reason for this suggestion is that many of the observed one-sided jet distributions of AGNs do not conform with that predicted if the one-sidedness is due solely to relativistic beaming—of the emission axis of the jet into a direction near the line of sight of the observer—wherein Doppler boosting of the radiation causes the approaching jet to be apparently brighter than the receding jet. Yet, up until the investigation reported here, no model has been proposed for the energy source that would exhibit such asymmetrical properties. Herein, however, from these Penrose scattering processes [5], I present evidence that the rotating black hole core energy source may be producing two of the important observed features of AGNs: the large energy fluxes of  $e^- e^+$  pairs inferred to emerge from their cores, and asymmetry in their jet and counter jet distributions. Moreover, findings by Dennett-Thorpe et al. [12], after studying the asymmetry of jets, lobe length, and spectral index in a sample of quasars, with well defined jets, led them to conclude that the simplest models of relativistic beaming fail to explain the “present observations”; and that only if the intrinsic spectrum is curved (i.e., with the spectral index increasing with frequency), such that the approaching lobe is seen at a significant lower frequency, will asymmetry of the right sense be produced. This somewhat supports the findings presented here, that asymmetry in the jet and counter jet is intrinsic to the energy source, suggesting that, relativistic beaming may just serve as an important enhancement mechanism. Further, recent observations of so-called microquasars in our Galaxy show some asymmetry in the jet and counter jet distributions [13]; and not all of the observed asymmetry can be explained by relativistic beaming,

suggesting that some asymmetry is intrinsic [14].

The remaining structure of this paper is as follows: In Section II, I present general formalisms and descriptions of the Kerr metric, particle orbits, the Penrose Compton scattering (PCS), the Penrose  $\gamma$ -ray— $\gamma$ -ray pair production [PPP ( $\gamma\gamma \rightarrow e^-e^+$ )], and the gravitomagnetic field (GM). Presented in Section III is a discussion of the gravitomagnetic field as it relates specifically to PCS and PPP ( $\gamma\gamma \rightarrow e^-e^+$ ). Finally, in Section IV, I conclude with an overview, including general discussions of how well these model results agree with astronomical observations, and the role of an external accretion disk magnetic field. Also, suggestions are made for further investigations.

## II. FORMALISM

### A. The Kerr Metric and Particle Orbits

For completeness, review, and to be referred to in the following sections, the spacetime separation between events near the KBH is defined by the Kerr metric [15]. The Kerr metric written in Boyer-Lindquist coordinates [16] and in geometrical units ( $G = c = 1$ ) is

$$ds^2 = -e^{2\nu} dt^2 + e^{2\psi} (d\Phi - \omega dt)^2 + e^{2\mu_1} dr^2 + e^{2\mu_2} d\Theta^2, \quad (1)$$

with

$$e^{2\nu} = \frac{\Sigma\Delta}{A}, \quad (2)$$

$$e^{2\psi} = \sin^2\Theta \frac{A}{\Sigma}, \quad (3)$$

$$e^{2\mu_1} = \frac{\Sigma}{\Delta}, \quad (4)$$

$$e^{2\mu_2} = \Sigma, \quad (5)$$

$$\omega = \frac{2Mar}{A}, \quad (6)$$

where

$$A \equiv (r^2 + a^2)^2 - a^2\Delta \sin^2\Theta, \quad (7)$$

$a$  is the angular momentum per unit mass parameter,  $M$  is the mass of the black hole, and  $\omega$  gives the frame dragging velocity. The quantities  $\Delta$  and  $\Sigma$  are defined by

$$\Delta \equiv r^2 - 2Mr + a^2 \quad (8)$$

and

$$\Sigma \equiv r^2 + a^2 \cos^2\Theta, \quad (9)$$

respectively. In general, the parameter  $a$  can have values  $0 \leq (a/M) \leq 1$ , values which allow for the existence of an event horizon. For a KBH, the event horizon is located at  $r = r_+ = M + (M^2 - a^2)^{1/2}$ , the larger root of the equation  $\Delta = 0$ . Here, in these Penrose processes, a canonical KBH is used, with its limiting value  $a/M = 0.998$ , as defined in [17], in the investigation of an accretion disk around a KBH. It is found that, if  $a/M$  is initially very close to 1 ( $0.999 \leq a/M \leq 1$ ), a small amount of accretion ( $\Delta M/M \leq 0.05$ ) through a disk quickly spins the hole down to a limiting state  $a/M \simeq 0.998$ . Conversely, if  $a/M$  is initially below this limiting value, accretion spins the hole up toward it.

Upon approaching a KBH from infinity, a limit is reached where the angular momentum of the KBH causes inertial frames to be dragged around in the direction that the black hole rotates. This limit is characterized by the vanishing of the  $g_{tt}$  component in Eq. (1):

$$g_{tt} = -\left(1 - \frac{2Mr}{\Sigma}\right) = 0. \quad (10)$$

More precisely, this limit is the larger root of  $g_{tt}$ , given analytically by

$$r = r_o = M + \left( M^2 - a^2 \cos^2 \Theta \right)^{1/2}. \quad (11)$$

The region between this limit and the event horizon is called the ergosphere.

Inside the ergosphere, the Kerr metric in the Boyer-Lindquist coordinate frame (BLF), i.e., frame of the observer at infinity, does not allow an observer to be stationary (in the sense of the observer being at rest with  $r, \Theta, \Phi = \text{constant}$ ) because of the dragging of inertial frames. For this reason, physical processes are difficult to describe in the BLF. In order to examine physical processes inside the ergosphere, Bardeen, Press, and Teukolsky [7] devised a frame of reference called the local nonrotating frame (LNRF). Observers in this frame rotate with the KBH in such away that the frame dragging effect of the rotating black hole is canceled as much as possible. In the LNRF, special relativity applies since locally spacetime has Lorentz geometry. The transformation laws, for the covariant components of a four-momentum, between the BLF and the LNRF tetrads are given in [3,5]. Note, in the LNRF,  $g_{\mu\nu} = \eta_{\mu\nu} \equiv$  Minkowski metric components.

However, it is better to use the BLF when describing the general orbits of particles (including photons) near the event horizon of the KBH. The BLF admits three constants of motion as measured by an observer at infinity [18]. In terms of the covariant components of the particle's four-momentum  $[P_\mu = (P_r, P_\Theta, P_\Phi, P_t); (\mu = r, \Theta, \Phi, t)]$  at some instant of time, the conserved quantities are  $E = -P_t \equiv$  total energy,  $L = P_\Phi \equiv$  component of the angular momentum parallel to the symmetry axis, and

$$Q = P_\Theta^2 + \cos^2 \Theta \left[ a^2 \left( \mu_o^2 - E^2 \right) + \frac{L^2}{\sin^2 \Theta} \right], \quad (12)$$

where  $\mu_o$  is the rest mass energy of the particle, which is a trivial fourth constant of motion. ( $Q$  is sometimes referred to as Carter's constant.) The value of  $Q$  is zero for particles whose motions are confined to the equatorial plane. The nonzero values of  $Q$  belong to particles which are moving in the  $\pm \hat{\mathbf{e}}_\Theta$  direction and/or are not confined to the equatorial plane.

The general expressions for the conserved energy  $E$  and azimuthal angular momentum  $L$  of massless ( $\mu_o = 0$ ) and material particles on orbits not confined to the equatorial plane (i.e., with  $Q > 0$ ) in the curved spacetime of a KBH are given below. For direct orbits of constant radius  $r$  [5]

$$E = \left( \frac{r^2 L^2 + D + F}{G} \right)^{1/2}, \quad (13)$$

and

$$P_\Phi = L = \left[ \frac{-J - (J^2 - 4IK)^{1/2}}{2I} \right]^{1/2}, \quad (14)$$

where

$$\begin{aligned} I &\equiv \frac{\tilde{A}^2 r^4}{G^2} - \frac{r^2}{G} (2\tilde{A}C + B^2) + C^2, \\ J &\equiv \frac{(D+F)}{G} \left[ \frac{2\tilde{A}^2 r^2}{G} - 2\tilde{A}C - B^2 \right] + 2\Delta (r^2 \mu_o^2 + Q) \left[ C - \frac{\tilde{A} r^2}{G} \right], \\ K &\equiv \frac{\tilde{A}^2}{G^2} (D+F)^2 - \frac{2\tilde{A}\Delta}{G} (r^2 \mu_o^2 + Q) (D+F) + \Delta^2 (r^2 \mu_o^2 + Q)^2; \end{aligned}$$

and

$$\begin{aligned} \tilde{A} &\equiv [(r^2 + a^2)^2 - a^2 \Delta], \\ B &\equiv 4Mar, \\ C &\equiv \Delta - a^2, \\ D &\equiv (3r^4 - 4Mr^3 + a^2 r^2) \mu_o^2, \\ F &\equiv (r^2 - a^2) Q, \\ G &\equiv 3r^4 + a^2 r^2. \end{aligned}$$

Note that, when  $Q = 0$ , Eqs. (13) and (14) reduce to the equations for equatorially confined orbits given in [7,5]. The quantity  $\sqrt{Q}$  ( $\equiv P_\Theta$ ) versus the conserved energy  $E$  [Eq. (13)] is plotted in Fig. 1(a) for the photon orbit at the radius  $r_{\text{ph}}$ , and in Fig. 1(b) for the electron orbits at the marginally bound and the marginally stable radii,  $r_{\text{mb}}$  and  $r_{\text{ms}}$ , respectively (these radii are discussed further in Sections II B and II C). Importantly, the derivations of Eqs. (13) and (14), derived in [5], now allow for Penrose processes be investigated in a practical way. That is, the motion of particles, above or below the equatorial plane (in the  $\pm\hat{e}_\Theta$  direction), can now be considered for the target particles as well as for the scattered particles, with  $E$  and  $L$  given separately by Eqs. (13) and (14), respectively, wherein  $Q$  is the independent variable for a specific black hole of mass  $M$  and angular momentum parameter  $a$ , at constant radius  $r$ .

When  $Q > 0$ , Eqs. (13) and (14) describe nonequatorially confined “spherical-like” orbits [19]. One of these spherical-like orbits, near the event horizon, consists of a particle repeatedly passing through the equatorial plane while tracing out a helical belt lying on a sphere at constant radius. The belt width between the maximum and minimum latitudes that the particle achieves, in general, increases with increasing  $Q$ , where  $Q$  is given by Eq. (12). In these spherical-like orbits, which in the limit of large radius goes asymptotically to a Keplerian circle, as the orbital radius approaches that of the event horizon, the dragging of the line of nodes, in the sense of the spin of the black hole, increases without limit. (The nodes are points at which the orbit, in going between negative and positive latitudes, intersects the equatorial plane.) Inside the ergosphere, during the time that a particle makes one oscillation in latitude, it will be swept through many complete azimuthal revolutions. Consequently, an orbit near the event horizon will have a helix-like shape with the axis parallel to the spin of the KBH. In the Penrose processes investigated here, it is assumed that a collision takes place, for a given observer, when the target particle with  $Q > 0$  passes through one of the nodes.

After the scattering events, not all of the particles escape to infinity. There are certain conditions that a particle must satisfy in order for it to be on an outgoing orbit. A thorough discussion of the escape conditions for material and massless particles is given in [5]. Generally speaking, these escape conditions compare the four-momentum components  $E'$ ,  $L'$ , and  $P'_\Theta$  ( $\equiv \sqrt{Q'}$ ) of the scattered particle to the values  $E$ ,  $L$ , and  $Q$  of a possible turning point, to see if the particle is on an escaping orbit. The expressions for  $E$  and  $L$  are given by Eqs. (13) and (14). Note that, for the nonequatorially confined ( $Q > 0$ ) spherical-like orbits, bound particles can have energies  $E/\mu_o > 1$ , because of an additional escape condition that must be satisfied.

## B. Penrose Compton Scattering (PCS)

In the PCS process, a photon of initial energy  $E_{\text{ph}}$ , as measured by an observer at infinity (i.e., in the BLF), is assumed to be emitted inside the ergosphere—emitted from the innermost region of the accretion disk, and follows a null geodesic trajectory before colliding with an equatorial or a nonequatorially confined orbiting electron, located at a specific radius of energy  $E_e$  and azimuthal momentum  $L_e [= (P_e)_\Phi]$  given by Eqs. (13) and (14), respectively. The motions of the incoming or incident photons considered in these scattering processes are those moving radially inward along the equatorial plane, as in [3]. Now, some of the photons, after being scattered by the electrons, eventually escape to infinity. For the scattered photons that are allowed to escape to infinity, an observer there would observe a low-energy (in most cases  $< \mu_e$ , where  $\mu_e$  is the electron rest mass energy) photon being scattered by a direct orbiting electron, after which the photon comes out with a higher energy (inverse Compton scattering). Subsequently, the target electron may recoil to another direct orbit of lesser energy, or the electron may be put on a retrograde orbit of negative energy. In both cases, the target electron gives up energy as measured by an observer at infinity. However, to a particular observer in the LNRF this is just a normal Compton scattering process in which the photon loses energy to the electron, since the photon arrives at this local frame with initial energy higher than  $\sim \mu_e$  [5]. The infall of the final negative energy electron results in an observer at infinity measuring a decrease in the rotational energy of the KBH. This inverse Compton scattering process is different from its flat spacetime counterpart. In the flat spacetime process, cold photons are heated by hot electrons to the temperature of the electrons. In the Penrose process, which occurs in the ergosphere, generally, photons are heated by the rotational energy of the black hole and the curvature of spacetime [3].

The conditions that the infalling photon encounters in its free fall through the ergosphere before arriving at the designated scattering radius are ignored in these calculations. Otherwise, conditions such as the particle density in the ergosphere and radiative transfer effects would have to be incorporated into the calculations along the null geodesic of the photon. It is assumed that these conditions cause little qualitative change in the results. The validity of this assumption can be found in [4], where it is shown that the variation in the density distribution does little to change the energies of the escaping photons. The photon arrives at the radius in which the scattering take place with an initial covariant four-momentum  $(P_{\text{ph}})_\mu = [(P_{\text{ph}})_r, (P_{\text{ph}})_\Theta, L_{\text{ph}}, -E_{\text{ph}}]$ , as measured by an observer at infinity. For a

photon falling radially inward along the equatorial plane,  $(P_{\text{ph}})_{\Theta} = L_{\text{ph}} = 0$ .

The initial energies  $E_{\text{ph}}$ , used in the model calculations presented here, are monochromatic for a given distribution of 2000 incident infalling photons. One scattering event per photon is assumed. The energies of the incident photons (0.511 MeV–1 MeV) are consistent with the bistable two-temperature accretion disk [8,20,21], referred to as the thin disk/ion corona accretion model (see [5] for further details concerning the disk model and the use of thermal initial particles).

The spatial distribution of the target electrons is assumed to be specified as circular orbiting rings of completely ionized plasma. Two radii are considered for the model electron rings:  $r_{\text{ms}}$  ( $\simeq 1.2M$ ), the radius of the marginally stable circular orbit and  $r_{\text{mb}}$  ( $\simeq 1.089M$ ), the radius of the marginally bound circular orbit, for a canonical KBH ( $a/M = 0.998$ ). Note that, the outer ergosphere boundary, the photon orbit, and the event horizon of a canonical KBH are located at  $r_o = 2M$ ,  $r_{\text{ph}} \simeq 1.074M$ , and  $r_+ \simeq 1.063M$ , respectively, in the equatorial plane. The region between the radii  $r_{\text{ms}}$  and  $r_{\text{mb}}$  represents the innermost possible periastrons (radial turning points) for bound unstable orbiting material particles. If given a sufficiently large inward perturbation, a particle in this region will eventually fall through the event horizon. Moreover,  $r_{\text{mb}}$  is the minimum periastron of all bound orbits of material particles, before plunging directly into the black hole.

After some manipulations of the results given in [5], eq. (3.47), the final four-momentum components of the PCS photon as measured by a BLF observer, can be expressed by the following:

$$E'_{\text{ph}} = \varepsilon_{\text{ph}}^{R'} \left\{ \gamma_e (e^\nu + \omega e^\psi \beta_\Phi) + \left[ \gamma_e e^\nu \beta_\Phi + \omega e^\psi \left( 1 + \beta_\Phi^2 \frac{\gamma_e^2}{\gamma_e + 1} \right) \right] \left( \cos \theta_{\text{ph}}^R \cos \delta^R + \sin \delta^R \sin \theta_{\text{ph}}^R \cos \alpha^R \right) \right\}, \quad (15)$$

$$(P'_{\text{ph}})_r = e^{\mu_1} \varepsilon_{\text{ph}}^{R'} \sin \theta_{\text{ph}}^{R'} \cos \left[ \pi - \arccos \left( \frac{\cos \delta^R - \cos \theta_{\text{ph}}^R \cos \theta_{\text{ph}}^{R'}}{\sin \theta_{\text{ph}}^R \sin \theta_{\text{ph}}^{R'}} \right) \right], \quad (16)$$

$$(P'_{\text{ph}})_{\Theta} = e^{\mu_2} \varepsilon_{\text{ph}}^{R'} \sin \theta_{\text{ph}}^{R'} \sin \left[ \pi - \arccos \left( \frac{\cos \delta^R - \cos \theta_{\text{ph}}^R \cos \theta_{\text{ph}}^{R'}}{\sin \theta_{\text{ph}}^R \sin \theta_{\text{ph}}^{R'}} \right) \right], \quad (17)$$

$$L'_{\text{ph}} = e^\psi \varepsilon_{\text{ph}}^{R'} \left[ \left( 1 + \beta_\Phi^2 \frac{\gamma_e^2}{\gamma_e + 1} \right) \left( \cos \theta_{\text{ph}}^R \cos \delta^R + \sin \delta^R \sin \theta_{\text{ph}}^R \cos \alpha^R \right) + \gamma_e \beta_\Phi \right], \quad (18)$$

where  $e^\nu$ ,  $e^\psi$ ,  $e^{\mu_1}$ ,  $e^{\mu_2}$ , and  $\omega$  are given by Eqs. (2) through (6); the other parameters will be defined in the following paragraph. These four-momentum components result from scattering off equatorial target electrons (i.e., targets confined to the equatorial plane). See [5] to derive the general expressions for both equatorial and nonequatorially confined targets. Note that, the arccosine term in Eqs. (16) and (17) defines an angle between 0 and  $2\pi$ .

The other parameters in the above four-momentum components [Eqs. (15) through (18)] are defined as follows [5]: For equatorial orbiting target electrons,  $\vec{\beta}_e = (\beta_r, \beta_\Theta, \beta_\Phi) = [0, 0, (v_e)_\Phi]$ , and  $\gamma_e = (1 - \beta_e^2)^{-1/2}$ , with

$$(v_e)_\Phi = \beta_\Phi = \frac{L_e e^{\nu-\psi}}{E_e - \omega L_e}, \quad (19)$$

where  $E_e$  and  $L_e$  are the conserved energy and azimuthal angular momentum as measured by an observer at infinity, given by Eqs. (13) and (14), respectively, of course with  $Q_e = 0$  for equatorially confined targets ( $Q_e \neq 0$  for nonequatorially confined targets);  $(v_e)_\Phi$  is the orbital velocity of the electron relative to the LNRF. Note that, in [5], I refer to the lab frame (LF) as the frame of a general observer in the LNRF; here I simply refer to it as the LNRF. The final energy of the PCS photon  $\varepsilon_{\text{ph}}^{R'}$ , as measured by an observer in the electron rest frame (ERF), is given by the familiar expression for Compton scattering in flat spacetime (see [5]):

$$\begin{aligned} \varepsilon_{\text{ph}}^{R'} &= \frac{\varepsilon_{\text{ph}}^R}{1 + (\varepsilon_{\text{ph}}^R / \mu_e)(1 - \cos \delta^R)} \\ &= \frac{\gamma_e e^{-\nu} E_{\text{ph}}}{1 + (\gamma_e e^{-\nu} E_{\text{ph}} / \mu_e)(1 - \cos \delta^R)}, \end{aligned} \quad (20)$$

where  $\varepsilon_{\text{ph}}^R$  is the initial energy of the photon in the ERF;  $\delta^R$  is the angle between the initial and final space momentum vectors of the photon in the ERF. The ERF and the LNRF are related by a Lorentz transformation, with relative frame velocity  $(v_e)_\Phi$ . The initial and final polar angles,  $\theta_{\text{ph}}^R$  and  $\theta_{\text{ph}}^{R'}$ , of the incoming and scattered photon space vectors, respectively, in the ERF [in which the coordinate system is centered on the electron at rest, with the polar axis  $(+\hat{\mathbf{e}}_{\mathbf{z}})$  of this Lorentz frame pointed in the positive  $\hat{\mathbf{e}}_{\Phi}$  direction of the BLF; see eqs. (3.3), (3.5), (3.6), (3.21), and (3.24) of [5]], are found to be

$$\begin{aligned}\theta_{\text{ph}}^R &= \arctan \left\{ \frac{[(p_{\text{ph}}^R)_r]^2 + (p_{\text{ph}}^R)_\Theta]^2}{(p_{\text{ph}}^R)_\Phi} \right\}^{1/2} \\ &= \pi - \arctan \left( \frac{1}{\gamma_e \beta_\Phi} \right) \\ &= \pi - \arctan \left[ \frac{2 m_e^2 M a r \sin^2 \Theta}{\omega L_e^2 (r^2 + a^2 \cos^2 \Theta)} \right]^{1/2}\end{aligned}\quad (21)$$

[using  $(p_{\text{ph}}^R)_r = -e^{-\nu} E_{\text{ph}}$ ,  $(p_{\text{ph}}^R)_\Theta = 0$ ,  $(p_{\text{ph}}^R)_\Phi = -\gamma_e \beta_\Phi e^{-\nu} E_{\text{ph}}$ , and eqs. (2.3), (2.10b), (2.12), (3.15) from [5]]; and

$$\theta_{\text{ph}}^{R'} = \arccos(\cos \theta_{\text{ph}}^R \cos \delta^R + \sin \delta^R \sin \theta_{\text{ph}}^R \cos \alpha^R) \quad (22)$$

[see also the azimuthal angle  $\phi_{\text{ph}}^{R'}$  [eq. (3.39)] of [5], given again here as Eq. (44)], where  $(p_{\text{ph}}^R)_r$ ,  $(p_{\text{ph}}^R)_\Theta$ , and  $(p_{\text{ph}}^R)_\Phi$  are the initial space momentum components of the photon in the ERF; note, the  $\pi$  term has been properly added since  $(p_{\text{ph}}^R)_\Phi < 0$ . The angles  $\theta_{\text{ph}}^{R'}$ ,  $\phi_{\text{ph}}^{R'}$  define the direction of the space momentum vector of the scattered photon in the ERF (see eq. (3.24) of [5]). The angles  $\delta^R$  and  $\alpha^R$  are the polar and azimuthal angles of the PCS photon relative to the direction of the initial photon: these angles are found by applying the Monte Carlo method to the Klein-Nishina cross section in the ERF (as done in [5]). Equations (21) and (22) will be important in the discussions of the GM field, in Sections II D and III, because of the frame dragging term  $\omega$  contained in  $\theta_{\text{ph}}^R$  [cf. Eqs. (15) through (18), (19), (21)], and (22)].

In [5], I present numerous cases of the obtained four-momentum spectra of the PCS photons. Below in Section III, however, I present only spectra that are relevant to the discussion at hand—i.e., of how the GM field affects the distributions of the scattered photons. Note that, the conserved energies  $E_e$  and angular momenta  $L_e$  of the nonequatorially confined target electrons, assumed in these calculations, are consistent with the electrons produced in Eilek's hot accretion disk model [8,20], described in details in [5]. The  $Q_e$  values used in Eqs. (13) and (14) for the nonequatorially confined target electrons correspond to orbits with polar latitudinal angles  $\lesssim 30^\circ$ , above and below the equatorial plane, consistent with what would be expected in thin disk/ion corona (or torus) accretion models.

### C. Penrose Gamma Ray-Gamma Ray Pair Production (PPP)

This PPP ( $\gamma\gamma \rightarrow e^-e^+$ ) process consists of collisions inside the ergosphere between radially infalling photons [5] and circularly orbiting photons that are bound at the radius of the photon orbit [7]:

$$r_{\text{ph}} = 2M\{1 + \cos[(2/3) \arccos(-a/M)]\}, \quad (23)$$

where  $r_{\text{ph}}$  represents an unstable circular orbit. On such spherical-like orbits, a photon circles indefinitely; however, a small perturbation can cause the photon to either escape to infinity or fall into the black hole. This orbit is the innermost boundary of circular orbits for all particles. The initial energies assumed in these calculations as measured by an observer at infinity, for the infalling photon and the orbiting photon,  $E_{\gamma 1}$  and  $E_{\gamma 2}$ , respectively, should be in the following ranges to be consistent with energies produced by thin disk/ion corona models, and with energies satisfying the threshold energy conditions for these reactions to occur [5]:

$$3.5 \text{ keV} \lesssim E_{\gamma 1} \lesssim 50 \text{ keV} \quad \text{and} \quad 3.4 \text{ MeV} \lesssim E_{\gamma 2} \lesssim 4 \text{ GeV},$$

where  $E_{\gamma 2}$  is given by Eq. (13) for the appropriate chosen value of  $Q_{\gamma 2}$ . Note that, the target photons,  $E_{\gamma 2}$ , have orbits not confined to the equatorial plane. These nonequatorially confined orbits allow for the photon's energy at the photon orbit to be used in a feasible way, whereas, for equatorially confined orbits, Eqs. (13) and (14), for  $E$  and

$L$ , respectively, equal zero [cf. Fig. 1(a)]. Or expressed in conventional terms,  $E$  and  $L$ , when  $Q=0$ , define the orbit of infinite energy and infinite azimuthal angular momentum per unit rest mass energy, respectively [7,5].

The high energy range for  $E_{\gamma 2}$  is chosen based on physical processes found to occur in the two-temperature bistable thin disk/ion corona accretion flow. More recently such type ion corona accretion flows have been called advection dominated accretion flows (ADAFs). ADAFs were predicted in Lightman's speculation of what might take place as a result of thermal and density instabilities [22]. These instabilities can cause the thin disk to form high and low density rings in the inner region and an increase in temperature from  $\sim 10^{5-7}$  K to  $\sim 10^{9-12}$  K [8,20,21,22]. Astrophysicists over the years, since Lightman's time-dependent disk model calculation of the early 1970s [22], and subsequent models [8,20], have continued to find properties of ADAFs [23]. The most important is the proton-proton collisions in which neutral pions  $\pi^0$  are emitted [8,20,23]. The neutral pion  $\pi^0$  subsequently decays into two energetic  $\gamma$ -rays with energies up to  $\sim 100$  MeV if the protons are assumed to have a blackbody distribution, or higher for an assumed power-law distribution [23]. Such photons could populate the photon orbit. These infalling photons would be blueshifted in energy-momentum at the photon orbit by a factor  $\sim e^{-\nu} \simeq 52$  (due to the rotating black hole producing the Lense-Thirring effect), where  $e^{-\nu}$  is the so-called blueshift factor given by Eq. (2) [cf. eq. (2.8d) of [5]]. This means that high energies up to  $\sim 5$  GeV (or higher) can possibly exist in the ergosphere at or near the photon orbit. However, it requires a process, such as the Penrose mechanism, to inject these highly blueshifted *trapped* orbiting photons into escaping orbits [7]—in this PPP ( $\gamma\gamma \rightarrow e^-e^+$ ), they escape in the form of energetic  $e^-e^+$  pairs. Moreover, it is well known that for rotating black holes with  $a/M = 0.998$ , the accretion disk extends inward to  $\sim r_{\text{ms}} (\simeq 1.2M)$ , inside of the radius of the ergosphere ( $r_o = 2M$ ). So, the  $\gamma$  rays produced in Eilek's hot accretion disk model [8,20], from the decay of neutral pions  $\pi^0 \rightarrow \gamma\gamma$ , described in details in [5], with energies peaked around  $\sim 75$  MeV, could very well be seed photons for these  $\gamma\gamma \rightarrow e^-e^+$  reactions, photons that have become blueshifted and bound at the photon orbit [24]. In addition, the PCS processes of [5] show that some of the scattered photons can also be seed particles for these reactions. Further, these photon collisions can occur at other radii besides the photon orbit, at, say another turning point, thereby increasing the probability of a collision. Again, it is important to point out that once the photons have been blueshifted to energies given by  $E_{\gamma 2}$ , and become bound at the photon orbit, they have no other way of escaping, except by some perturbing physical interaction, such as these PPP ( $\gamma\gamma \rightarrow e^-e^+$ ) processes. Note that, in [5], these PPP ( $\gamma\gamma \rightarrow e^-e^+$ ) processes are defined as *quasi*-Penrose processes since they are somewhat different from classical Penrose processes—which utilize the retrograde orbits of particles in the ergosphere.

Before proceeding, I want to discuss the assumptions made above and their validities. First, it is assumed that the blueshift in the energy of an infalling orbiting particle as measured by a LNRF observer is approximately equal to that measured by a BLF observer. This is a valid assumption because, for a particle in a circular bound orbit about the KBH, there is little difference between the energy measured locally in the LNRF [eq. (2.8d) of [5]] and that measured by an observer at infinity (i.e., in the BLF) [Eq. (13)]; for example, at the photon orbit  $r_{\text{ph}}$ , the ratio of the energy measured by an observer in the LNRF,  $\varepsilon_{\text{ph}}^*$ , to that measured by an observer in BLF,  $E_{\text{ph}}^*$ , is  $\simeq 1.055$ . Second, it is assumed that the photons populating the photon orbit have been created by some prior processes (disk instability and/or Penrose), which yielded them with appropriate energies and momenta. We know from [5] that the condition

$$\eta'_{\text{ph}} \geq \eta_{\text{ph}}^* \equiv \frac{Q'_{\text{ph}}}{E'^2_{\text{ph}}} \geq \frac{Q_{\text{ph}}^*}{E_{\text{ph}}^{*2}}$$

guarantees the existence of a turning point outside the event horizon for which the radial motion goes to zero and changes direction for photons emitted not confined to the equatorial plane [i.e.,  $(P'_{\text{ph}})_{\Theta} \neq 0$ ]. The asterisks indicate the nonequatorially confined circular photon orbit, where  $r = r_{\text{ph}}$  [see Eq. (23)], which is a potential turning point, and the primes indicate a photon resulting from some prior process, say PCS. Once the condition above has been met, indicating the existence of a turning point outside the horizon, to find out whether or not the photon orbit is a true turning point, for a particular photon, it seems plausible to set  $Q'_{\text{ph}} = Q_{\text{ph}}^*$ , in the the condition above, and let  $E'_{\text{ph}} \rightarrow e^{-\nu} E'_{\text{ph}} \equiv E''_{\text{ph}}$ , as the photon travels inward toward the photon orbit, obtaining the requirement that  $E''_{\text{ph}} \leq E_{\text{ph}}^*$  for the existence of a turning point at  $r = r_{\text{ph}}$  [where, again,  $e^{-\nu}$  is the blueshift factor given by Eq. (2), due to the local inertial frame dragging or Lense-Thirring effect; cf. also Eq. (1)]. After the photon has reached its turning point, it escapes outward with “redshifted” energy given by  $E'_{\text{ph}} = e^{\nu} E''_{\text{ph}}$  as measured by an observer at infinity, i.e., in the BLF. Notice that the condition above is independent of  $L'_{\text{ph}}$ . The other condition that independently guarantees the existence of a turning point in  $P_r$ , however, for photons confined to escape along the equatorial plane, as well as for those escaping not confined to the equatorial plane, involves  $L'_{\text{ph}}$ ; see [5] for details. In [5], it is found that many of the PCS photons have appropriate  $E'_{\text{ph}}$  and  $Q'_{\text{ph}}$  values to populate the turning point trajectories at or near the photon orbit [cf. Figs. 3 and 4 to Fig. 1(a)]. Because of this, it is not unreasonable to expect the photons produced by the  $\pi^0 \rightarrow \gamma\gamma$  decays (discussed above) to acquire appropriate  $E'_{\text{ph}}$  and  $Q'_{\text{ph}}$  values, particularly, if the process, starting from the proton-proton scattering, is properly considered as a Penrose process

inside the ergosphere. Note, the radii of other turning points can be found from Eqs. (13) and (14), by satisfying the condition  $E''_{\text{ph}} \equiv e^{-\nu} E'_{\text{ph}} \leq E^*_{\text{ph}}$ , for the specified “iso- $Q$ ” value orbit ( $\equiv$  circular orbit of equal  $Q$ ), where now the radius of the turning point can exist anywhere near the event horizon, say between  $r_{\text{mb}} > r > r_{\text{ph}}$  for the inward PCS photons. This means that such photons satisfying the condition for the existence of a turning point can have energies at these turning points corresponding to blueshift factors in the range of  $32 < e^{-\nu} < 52$ . The largest factors, however, will be for photons nearest the photon orbit. In these calculations, the investigation centers around those photons with turning points at the photon orbit where the highest energy can be extracted. Yet, consideration of all of the possible turning points will increase the probability of a PPP ( $\gamma\gamma \rightarrow e^-e^+$ ) process occurring, as mentioned earlier, giving rise to a larger volume of  $e^-e^+$  pairs. Moreover, no null geodesic has more than one turning point in its radial motion outside the event horizon (see [5] for details and a complete description of escape conditions). Further, one way to described particles trajectories in the ergosphere is the following: As a particle travels with  $P_r > 0$  or  $P_r < 0$  to, say  $P_r = 0$ , all local inertial frames as measured by an observer at infinity, i.e., in the BLF, are dragged into rotation by the KBH, irrespective of the four-momentum of the particle as it moves relative to local or neighboring inertial frames. (Note, particles could also be undergoing local relativistic scatterings as in the Penrose processes considered here.) The BLF observer measures the effects, given by  $P_\mu = (P_r, P_\Theta, L, -E)$ , of this frame dragging on the particle as it moves in such a strong gravitational environment (more on this in Section III A).

Now proceeding, manipulations of the results given in [5] yield, in the following form, the final four-momentum components of the PPP positron ( $e^+$ ) and negatron ( $e^-$ ) as measured by an observer in the BLF:

$$\begin{aligned}
E_+ = e^\nu \gamma_{\text{c.m.}} & \left\{ \varepsilon_+^c + \left( \varepsilon_+^{c^2} - \mu_e^2 \right)^{1/2} \left[ (\beta_{\text{c.m.}})_r \sin \theta_{e^+}^c \cos \phi_{e^+}^c \right. \right. \\
& \left. \left. + (\beta_{\text{c.m.}})_\Theta \sin \theta_{e^+}^c \sin \phi_{e^+}^c + (\beta_{\text{c.m.}})_\Phi \cos \theta_{e^+}^c \right] \right\} + \omega e^\psi \left[ \left( \varepsilon_+^{c^2} - \mu_e^2 \right)^{1/2} \right. \\
& \left. \left\{ \frac{\gamma_{\text{c.m.}}^2}{\gamma_{\text{c.m.}} + 1} (\beta_{\text{c.m.}})_\Phi \left[ (\beta_{\text{c.m.}})_\Theta \sin \theta_{e^+}^c \sin \phi_{e^+}^c \right. \right. \right. \\
& \left. \left. + (\beta_{\text{c.m.}})_r \sin \theta_{e^+}^c \cos \phi_{e^+}^c \right] + \left[ 1 + (\beta_{\text{c.m.}})_\Phi^2 \frac{\gamma_{\text{c.m.}}^2}{\gamma_{\text{c.m.}} + 1} \right] \right. \\
& \left. \left. \cos \theta_{e^+}^c \right\} + \gamma_{\text{c.m.}} (\beta_{\text{c.m.}})_\Phi \varepsilon_+^c \right], \tag{24}
\end{aligned}$$

$$\begin{aligned}
(P_+)_r = e^{\mu_1} & \left[ \left( \varepsilon_+^{c^2} - \mu_e^2 \right)^{1/2} \left\{ \frac{\gamma_{\text{c.m.}}^2}{\gamma_{\text{c.m.}} + 1} (\beta_{\text{c.m.}})_r \left[ (\beta_{\text{c.m.}})_\Phi \cos \theta_{e^+}^c \right. \right. \right. \\
& \left. \left. + (\beta_{\text{c.m.}})_\Theta \sin \theta_{e^+}^c \sin \phi_{e^+}^c \right] + \left[ 1 + (\beta_{\text{c.m.}})_r^2 \frac{\gamma_{\text{c.m.}}^2}{\gamma_{\text{c.m.}} + 1} \right] \right. \\
& \left. \left. \sin \theta_{e^+}^c \cos \phi_{e^+}^c \right\} + \gamma_{\text{c.m.}} (\beta_{\text{c.m.}})_r \varepsilon_+^c \right], \tag{25}
\end{aligned}$$

$$\begin{aligned}
(P_+)_\Theta = e^{\mu_2} & \left[ \left( \varepsilon_+^{c^2} - \mu_e^2 \right)^{1/2} \left\{ \frac{\gamma_{\text{c.m.}}^2}{\gamma_{\text{c.m.}} + 1} (\beta_{\text{c.m.}})_\Theta \left[ (\beta_{\text{c.m.}})_\Phi \cos \theta_{e^+}^c \right. \right. \right. \\
& \left. \left. + (\beta_{\text{c.m.}})_r \sin \theta_{e^+}^c \cos \phi_{e^+}^c \right] + \left[ 1 + (\beta_{\text{c.m.}})_\Theta^2 \frac{\gamma_{\text{c.m.}}^2}{\gamma_{\text{c.m.}} + 1} \right] \right. \\
& \left. \left. \sin \theta_{e^+}^c \sin \phi_{e^+}^c \right\} + \gamma_{\text{c.m.}} (\beta_{\text{c.m.}})_\Theta \varepsilon_+^c \right], \tag{26}
\end{aligned}$$

$$(P_+)_\Phi = L_+ = e^\psi \left[ \left( \varepsilon_+^{c^2} - \mu_e^2 \right)^{1/2} \left\{ \frac{\gamma_{\text{c.m.}}^2}{\gamma_{\text{c.m.}} + 1} (\beta_{\text{c.m.}})_\Phi \right. \right.$$

$$\begin{aligned}
& \left[ (\beta_{\text{c.m.}})_{\Theta} \sin \theta_{e^+}^c \sin \phi_{e^+}^c + (\beta_{\text{c.m.}})_r \sin \theta_{e^+}^c \cos \phi_{e^+}^c \right] \\
& + \left[ 1 + (\beta_{\text{c.m.}})_{\Phi}^2 \frac{\gamma_{\text{c.m.}}^2}{\gamma_{\text{c.m.}} + 1} \right] \cos \theta_{e^+}^c \left. \vphantom{\left[ (\beta_{\text{c.m.}})_{\Theta} \sin \theta_{e^+}^c \sin \phi_{e^+}^c + (\beta_{\text{c.m.}})_r \sin \theta_{e^+}^c \cos \phi_{e^+}^c \right]} \right\} \\
& + \gamma_{\text{c.m.}} (\beta_{\text{c.m.}})_{\Phi} \varepsilon_+^c \left. \vphantom{\left[ (\beta_{\text{c.m.}})_{\Theta} \sin \theta_{e^+}^c \sin \phi_{e^+}^c + (\beta_{\text{c.m.}})_r \sin \theta_{e^+}^c \cos \phi_{e^+}^c \right]} \right], \tag{27}
\end{aligned}$$

where, again,  $e^\nu$ ,  $e^\psi$ ,  $e^{\mu_1}$ ,  $e^{\mu_2}$ , and  $\omega$  are given by Eqs. (2) through (6), however, evaluated at the photon orbit  $r_{\text{ph}}$  [Eq. (23)]. Note, sometimes I refer to the  $e^-e^+$  pairs as PPP electrons.

The other expressions in the above four-momentum components [Eqs. (24) through (27)] are defined as follows (just as in the PCS, these definitions are derived from [5]; the results are presented here). The subscript c.m. defines the center-of-momentum frame, and the superscript  $c$  indicates parameters measured relative to this frame. The c.m. frame and the LNRF are related by a Lorentz transformation, with relative frame velocity defined by  $\vec{\beta}_{\text{c.m.}} = \mathbf{v}_{\text{c.m.}} = [(\beta_{\text{c.m.}})_r, (\beta_{\text{c.m.}})_{\Theta}, (\beta_{\text{c.m.}})_{\Phi}]$ , and with the Lorentz factor of the c.m. frame given by  $\gamma_{\text{c.m.}} = (1 - \beta_{\text{c.m.}}^2)^{-1/2}$ . In general,

$$\vec{\beta}_{\text{c.m.}} = \frac{\mathbf{p}_{\gamma 1} + \mathbf{p}_{\gamma 2}}{\varepsilon_{\gamma 1} + \varepsilon_{\gamma 2}}, \tag{28}$$

where  $\varepsilon_{\gamma 1}$  and  $\mathbf{p}_{\gamma 1}$  are the energy and space momentum vector, respectively, of the radially infalling photon as measured by a LNRF observer;  $\varepsilon_{\gamma 2}$  and  $\mathbf{p}_{\gamma 2}$  are these measured quantities for the orbiting photon. Using eqs. (3.90)-(3.92), with  $\theta_{\gamma 1} = \pi/2$  and  $\phi_{\gamma 1} = \pi$ , and (2.8a)-(2.8c) of [5] in Eq. (28) above, and after some manipulation, we find that

$$\begin{aligned}
\vec{\beta}_{\text{c.m.}} &= [(\beta_{\text{c.m.}})_r, (\beta_{\text{c.m.}})_{\Theta}, (\beta_{\text{c.m.}})_{\Phi}] \\
&= (E_{\gamma 1} + E_{\gamma 2} - \omega L_{\gamma 2})^{-1} (-E_{\gamma 1}, e^{\nu - \mu_2} \sqrt{Q_{\gamma 2}}, e^{\nu - \psi} L_{\gamma 2}), \tag{29}
\end{aligned}$$

where  $E_{\gamma 1}$  and  $E_{\gamma 2}$  are the conserved initial energies of the infalling incident and target orbiting photons, respectively, measured in the BLF, and  $L_{\gamma 2}$  is the corresponding conserved azimuthal angular momentum of  $E_{\gamma 2}$ . The c.m. frame energy is given by [5]

$$\begin{aligned}
\varepsilon_+^c &= \sqrt{\frac{1}{2} \varepsilon_{\gamma 1} \varepsilon_{\gamma 2} (1 - \cos \theta_{\gamma \gamma})} \\
&= e^{-\nu} \sqrt{\frac{1}{2} E_{\gamma 1} (E_{\gamma 2} - \omega L_{\gamma 2})}, \tag{30}
\end{aligned}$$

where  $\theta_{\gamma \gamma}$  ( $= \pi/2$ ) is the polar angle between  $\mathbf{p}_{\gamma 1}$  and  $\mathbf{p}_{\gamma 2}$  in the LNRF. The polar and azimuthal angles ( $\theta_{e^+}^c, \phi_{e^+}^c$ ) of the  $e^+$  in the c.m. frame, with the polar axis of the coordinate system pointed in the positive  $\hat{\mathbf{e}}_{\Phi}$  direction, are given below in terms of the scattering angles ( $\theta_+^c, \phi_+^c$ ), which are found from application of the Monte Carlo method to the cross section for these pair production scattering events [5]:

$$\theta_{e^+}^c = -\arcsin \left( \frac{\cos \theta_+^c}{\cos \phi_{e^+}^c} \right); \tag{31}$$

$$\phi_{e^+}^c = \arctan \left[ \frac{-D_2 + (D_2^2 - 4D_1 D_3)^{1/2}}{2D_1} \right], \tag{32}$$

where

$$\begin{aligned}
D_1 &\equiv \cos^2 \theta_+^c \sin^2 \theta_+^c; \\
D_2 &\equiv 2 \cos \theta_+^c \sin \theta_+^c \sin \phi_+^c (1 - \cos^2 \theta_+^c); \\
D_3 &\equiv 1 + \cos^2 \theta_+^c (\cos^2 \theta_+^c - 2) + \sin^2 \theta_+^c \cos^2 \phi_+^c (\cos^2 \theta_+^c - 1).
\end{aligned}$$

The corresponding angles for the  $e^-$  are given by

$$\theta_{e^-}^c = \pi - \theta_{e^+}^c, \tag{33}$$

$$\phi_{e^-}^c = \phi_{e^+}^c + \pi. \tag{34}$$

Note that, to find the corresponding four-momentum components of Eqs. (24) through (27) for the  $e^-$ , change the subscripts to “-”, using the fact that  $\varepsilon_+^c = \varepsilon_-^c$ , and let  $\theta_{e^+}^c \rightarrow \theta_{e^-}^c$ ,  $\phi_{e^+}^c \rightarrow \phi_{e^-}^c$ , with the new angles defined by Eqs. (33) and (34) above. Equations (29) and (30) will be important in the discussion of the GM field in Sections II D and III, i.e., because of the frame dragging term  $\omega$  contained in these equations [cf. Eqs. (24) through (27), (29) and (30)].

Similarly, as for the PCS photons, numerous cases of the obtained four-momentum spectra of the PPP ( $\gamma\gamma \rightarrow e^-e^+$ ) electrons are presented in [5]. Below, in Section III, I present only spectra that are relevant to the discussion at hand of how the GM field affects the Penrose produced  $e^-e^+$  pairs.

#### D. The Gravitomagnetic (GM) Field

In order to understand and to appreciate the origin of the asymmetry in the distributions of the scattered particles in the polar ( $\Theta$ ) direction, mentioned in Section I, one must look in details at the gravitomagnetic (GM) force field [10]—the force responsible for the asymmetry. The gravitational force of a rotating body of mass consists of two parts, which are analogous to an electromagnetic field. The first part is the familiar gravitational force that a body of rotating or nonrotating mass  $M$  produces on a test particle of mass  $m$ :

$$\left( \frac{d\mathbf{p}}{d\tau} \right)_{\text{grav}} = \frac{m}{(1 - \mathbf{v}^2)^{1/2}} \mathbf{g}, \quad (35)$$

where the gravitational acceleration  $\mathbf{g}$  is produced by the gradient of the “redshift factor”  $e^\nu$  of Eq. (2); note, the inverse  $e^{-\nu}$  is referred to as the blueshift factor [5,9]:

$$\begin{aligned} \mathbf{g} &= -\nabla \ln e^\nu \\ &= -\frac{\Sigma M(r^4 - a^4) + 2Mr^2 a^2 \Delta \sin^2 \Theta}{A\sqrt{\Delta}\Sigma^3} \hat{\mathbf{e}}_r \\ &\quad + \frac{2Mra^2(r^2 + a^2)}{A\sqrt{\Sigma^3}} \cos \Theta \sin \Theta \hat{\mathbf{e}}_\Theta. \end{aligned} \quad (36)$$

The above force is analogous to the electric force field surrounding an electric charge source (i.e., like the Coulomb field between point charges), and for this reason is sometimes referred to as the “gravitoelectric” force.

The second part, however, is less familiar. It is the additional gravitational force that a rotating mass produces on a test particle. This force, called the GM force, is produced by the gradient of  $\vec{\beta}_{\text{GM}} = -\omega \hat{\mathbf{e}}_\Phi$ , where  $\omega$  ( $= -g_{\Phi t}/g_{\Phi\Phi}$  [7]) is the frame dragging velocity appearing in Eq. (1), expressed by Eq. (6). The GM force exerted on a test particle of space momentum  $\mathbf{p}$  is given by [10]

$$\left( \frac{d\mathbf{p}}{d\tau} \right)_{\text{GM}} = \overset{\leftrightarrow}{\mathbf{H}} \cdot \mathbf{p}, \quad \text{i.e.,} \quad \left( \left( \frac{d\mathbf{p}}{d\tau} \right)_{\text{GM}} \right)_i = H_{ij} p^j, \quad (37)$$

with

$$\overset{\leftrightarrow}{\mathbf{H}} \equiv e^{-\nu} \nabla \vec{\beta}_{\text{GM}}, \quad \text{i.e.,} \quad H_{ij} = e^{-\nu} (\beta_{\text{GM}})_{j|i}$$

(the vertical line indicates the covariant derivative in 3-dimensional absolute space). The field  $\overset{\leftrightarrow}{\mathbf{H}}$  is called the GM tensor field, and  $\vec{\beta}_{\text{GM}}$  is sometimes called the GM potential. The components of  $\overset{\leftrightarrow}{\mathbf{H}}$  in the LNRF are [10]

$$H_{\Theta\Phi} = -\frac{2aMr \cos \Theta}{\Sigma^2 \sqrt{A^3}} \left[ (r^2 + a^2)A + a^2 \Sigma \Delta \sin^2 \Theta \right] e^{-\nu} \equiv H^r,$$

$$H_{\Phi\Theta} = \frac{2aMr \cos \Theta}{\Sigma^2 \sqrt{A^3}} \left[ (r^2 + a^2)A - a^2 \Sigma \Delta \sin^2 \Theta \right] e^{-\nu} \equiv -\tilde{H}^r,$$

$$H_{r\Phi} = -\frac{2aM\sqrt{\Delta} \sin \Theta}{\Sigma^2 \sqrt{A^3}} \left\{ a^2 \cos^2 \Theta A - \Sigma r \left[ 2r(r^2 + a^2) \right. \right.$$

$$\left. -a^2(r - M) \sin^2 \Theta \right\} e^{-\nu} \equiv -\tilde{H}^\Theta,$$

$$H_{\Phi r} = -\frac{2aM\sqrt{\Delta}\sin\Theta}{\Sigma^2\sqrt{A^3}} \left\{ r^2 A - \Sigma r \left[ 2r(r^2 + a^2) \right. \right. \\ \left. \left. - a^2(r - M) \sin^2 \Theta \right] \right\} e^{-\nu} \equiv H^\Theta. \quad (38)$$

(The above definitions will become clearer in later sections.) Note that, like the magnetic Lorentz force  $\mathbf{f}_B = q(\mathbf{v} \times \mathbf{B})$ , on a particle of charge  $q$ , moving with velocity  $\mathbf{v}$ , in a magnetic field  $\mathbf{B}$ , the GM force of Eq. (37) vanishes when the particle is at rest.

The justification for the word “gravitomagnetic” becomes clear when we look at the GM force at a large distance from the event horizon ( $r \gg r_+$ ), exerted on a particle of mass  $m$  traveling with low velocity ( $v \ll c$ ). The GM force as measured by an observer at infinity [of whom I will refer to, after the introduction of Eq. (47), as the asymptotic rest BLF observer], under these conditions, is given by  $\mathbf{F}_{\text{GM}} \simeq m(\mathbf{v} \times \mathbf{H})$ , where  $\mathbf{H}$  is called the GM vector field—which contains the same information as the antisymmetric part of the GM tensor field [10]:

$$H^j \equiv \epsilon^{jkl} H_{kl} = \epsilon^{jkl} e^{-\nu} \nabla_k (\beta_{\text{GM}})_l; \quad \text{i.e., } \mathbf{H} \equiv e^{-\nu} \nabla \times \vec{\beta}_{\text{GM}},$$

or

$$\mathbf{H} = H^\Theta \hat{\mathbf{e}}_\Theta + H^r \hat{\mathbf{e}}_r \\ = -\frac{2aM}{\sqrt{\Sigma^5}} \left[ (r^2 - a^2 \cos^2 \Theta) \sin \Theta \hat{\mathbf{e}}_\Theta + \frac{2r(r^2 + a^2)}{\sqrt{\Delta}} \cos \Theta \hat{\mathbf{e}}_r \right]. \quad (39)$$

Thus, one sees that the GM force on a test particle of mass  $m$  is similar to the Lorentz magnetic force  $\mathbf{f}_B$  on a test particle of charge  $q$ , as given above, with the vectors  $\mathbf{H}$  and  $\mathbf{B}$  being analogous. In addition, the lines of force of  $\mathbf{H}$  have characteristics similar to that of a dipole magnetic field. Therefore, because of resemblances such as these (more examples given in [10]), of the force field produced by the mass and angular momentum of the rotating black hole, to that of a magnetic force field, thence came the term gravitomagnetic.

To assure a further understanding of the GM force field, one can think of it as the following. Just as the gravitational force causes local inertial frames to fall with acceleration  $\mathbf{g}$ , the GM field  $\mathbf{H}$  causes local inertial frames to rotate with angular velocity  $\vec{\Omega}_{\text{GM}} = -\mathbf{H}/2$ . In other words, the GM field  $\mathbf{H}$  can be thought of as a force field that drags local inertial frames into rotation and, as a result, produces a “Coriolis force”  $m(\mathbf{v} \times \mathbf{H})$  at  $r \gg r_+$ . The angular rotation velocity  $\Omega_{\text{GM}}$  is universally induced in all bodies and neighboring inertial frames, at a given radius, i.e., independent of the mass  $m$  of the body, just as in the case of  $\mathbf{g}$ .

Moreover,  $\vec{\Omega}_{\text{GM}}$  is equal to the precession rate of the spin  $\mathbf{s}$  of a gyroscope in the GM field of a rotating body [10]. The angular momentum of the gyroscope is changed by the torque  $d\mathbf{s}/dt = (1/2)\mathbf{s} \times \mathbf{H}$ , analogous to the torque  $\vec{\mu} \times \mathbf{B}$  exerted by a magnetic field  $\mathbf{B}$  on a magnetic dipole moment  $\vec{\mu}$  of a “test” magnet. Also, the precession rate  $\vec{\Omega}_{\text{GM}}$ , like the acceleration of gravity  $\mathbf{g}$ , is independent of the composition and structure of the gyroscope. It is a universal precession induced in all bodies, even those with vanishingly small angular velocity.

The effect of inertial frame dragging, specifically that concerning the GM precession of gyroscopes, was discovered in the equations of general relativity by Thirring and Lense in 1918 [1] and, thus, is often called the Lense-Thirring effect. Since there has not yet been a detection of the GM field of any rotating body [10]—and to date this still may be the case, it would be another significant test of general relativity, if we find, as these calculations suggest, that the one-sidedness in the jets of AGNs is due largely to the GM field.

I now use Eqs. (37) and (38) to evaluate the force experienced by a test particle under the influence of the GM field, as measured by a LNRF observer. In the LNRF, since the covariant components of a four-momentum vector  $\{p_\mu = [p_r, p_\Theta, p_\Phi, p_t (= -\varepsilon)]\}$  are related to the contravariant components by  $p^\mu = \eta^{\mu\nu} p_\nu$ , where  $\eta^{\mu\nu} \equiv$  Minkowski metric components, then the space components of the GM force, exerted on a test particle, are found to be

$$\left( f_{\text{GM}} \right)_r = -\frac{2aM\sqrt{\Delta}\sin\Theta}{\Sigma^2\sqrt{A^3}} \left\{ a^2 \cos^2 \Theta A - \Sigma r \left[ 2r(r^2 + a^2) \right. \right. \\ \left. \left. - a^2(r - M) \sin^2 \Theta \right] \right\} p_\Phi \equiv -\tilde{H}^\Theta p_\Phi, \quad (40)$$

$$\left(f_{\text{GM}}\right)_{\Theta} = -\frac{2aMr \cos \Theta}{\Sigma^2 \sqrt{A^3}} \left[ (r^2 + a^2)A + a^2 \Sigma \Delta \sin^2 \Theta \right] p_{\Phi} \equiv H^r p_{\Phi}, \quad (41)$$

and

$$\begin{aligned} \left(f_{\text{GM}}\right)_{\Phi} = & -\frac{2aM\sqrt{\Delta} \sin \Theta}{\Sigma^2 \sqrt{A^3}} \left\{ r^2 A - \Sigma r \left[ 2r(r^2 + a^2) \right. \right. \\ & \left. \left. - a^2(r - M) \sin^2 \Theta \right] \right\} p_r + \frac{2aMr \cos \Theta}{\Sigma^2 \sqrt{A^3}} \\ & \left[ (r^2 + a^2)A - a^2 \Sigma \Delta \sin^2 \Theta \right] p_{\Theta} \equiv H^{\Theta} p_r - \tilde{H}^r p_{\Theta}. \end{aligned} \quad (42)$$

(Again, the definitions will become clearer in later sections.) Even though these GM force components are what is measured locally, i.e., in the LNRF, they are sufficient for our purposes to describe what we observe at infinity, i.e., in the BLF, since the space momentum components in the LNRF ( $p_r, p_{\Theta}, p_{\Phi}$ ) and the BLF ( $P_r, P_{\Theta}, P_{\Phi}$ ) are related in a linear fashion (see the transformations between these frames given by eqs. (2.7) and (2.8) of [5]). Notice that the radial component  $(f_{\text{GM}})_r$  and the polar component  $(f_{\text{GM}})_{\Theta}$  [Eqs. (40) and (41)], exerted by the GM field, are proportional to the azimuthal momentum of the particle. This means that the absolute magnitudes of these force components will increase as the energy,  $E'$ , of the scattered particle increases, since  $P'_{\Phi}$  ( $= L'$ ) and  $E'$  increase linearly [5]. The azimuthal component  $(f_{\text{GM}})_{\Phi}$  of Eq. (42) will act according to the radial and polar momenta of the incident and scattered particles, exerting a force in the azimuthal ( $\Phi$ ) direction. This GM force component could be important in the polar collimation effects produced by the rotating black hole [25,26]; however, it is beyond the scope of this manuscript to discuss it in that context here.

Displayed in Figs. 2(a) and 2(b) are the ratios  $(f_{\text{GM}})_r/p_{\Phi}$  and  $(f_{\text{GM}})_{\Theta}/p_{\Phi}$ , respectively, as functions of the polar angle  $\Theta$ , which will be compared to the polar angle of escape for a Penrose scattered particle. The angle  $\Theta$  varies from 0 to  $\pi$ , with the equatorial plane located at  $\pi/2$ . For a given positive  $p_{\Phi}$ , as opposed to negative  $p_{\Phi}$  for retrograde motion, notice that  $(f_{\text{GM}})_r$  of Fig. 2(a) reaches a maximum in the equatorial plane, and increases with increasing  $r$  away from the event horizon, within the range of  $r$  considered. In Fig. 2(b), we notice that  $(f_{\text{GM}})_{\Theta}$  is antisymmetric, above and below the equatorial plane, and reaches negative and positive maxima at  $\Theta \sim 60^\circ$  and  $\Theta \sim 120^\circ$ , respectively. Moreover, the maximum value of the GM force component  $(f_{\text{GM}})_{\Theta}$  is larger than that of  $(f_{\text{GM}})_r$  by factors of  $\simeq 10.5$  and  $16.4$  at  $r_{\text{mb}}$  and  $r_{\text{ph}}$ , respectively, and the strength of  $(f_{\text{GM}})_{\Theta}$  decreases little with increasing  $r$  [cf. Fig. 2(a) and 2(b)]. Figure 2 will be discussed further in the following section.

### III. DISCUSSION: THE GM FIELD AND THE PENROSE PROCESSES

In this section, I use the results of the four-momenta of the Penrose scattered particles, found in [5], and presented again in Eqs. (15) through (18) and (24) through (27) showing specific details, to see what internal role the GM force of Eqs. (40) through (42) has in determining the spacial distributions of the Penrose scattered escaping particles. In the following, one must bear in mind that the GM force has already been accounted for in these Penrose processes (as done in the model calculations of [5]) through the Kerr metric tensor of Eq. (1), whose function is to describe the geodesics of the particles, on which the four-momentum is defined. That is, just as we do not have to calculate separately the gravitational force on the scattered particles [Eq. (35)], we do not have to calculate separately the GM force on the scattered particles [Eq. (37)], because both of these gravitational forces are inherently tied to the overall scattering process through the Kerr metric. The GM force, however, is given here separately only to show how it relates to the final four-momentum vectors of the scattered particles. Therefore, when looking at this force separately, in some instances, the precise relationship of the GM force with a distribution of scattered particles may not be clear. With this in mind we now proceed.

#### A. The Gravitomagnetic Field and PCS

Beginning with the PCS, displayed in Figs. 3–7 are scatter plots of the momentum components  $(P'_{\text{ph}})_r$  and  $(P'_{\text{ph}})_{\Theta}$  [see Eqs. (16) and (17)], and the corresponding polar angles  $\Theta'_{\text{ph}}$  [to be compared with  $\Theta$  in Eqs. (40) through (42)] of the escaping PCS photons. The polar angle (defined here as the angle of escape [3,4]) is given generally for a particle of type  $i$  by [25]

$$\Theta_i = \frac{\pi}{2} \mp \arccos \left[ \frac{-T + \sqrt{T^2 - 4SU}}{2S} \right]^{1/2}, \quad (43)$$

where

$$\begin{aligned} S &\equiv a^2(\mu_o^2 - E^2); \\ T &\equiv Q + a^2(E^2 - \mu_o^2) + L^2; \\ U &\equiv -L^2; \end{aligned}$$

the negative and positive signs are for particles traveling above or below the equatorial plane, respectively. The polar angle of Eq. (43) is derived from Eq. (12) by letting  $P_\Theta \rightarrow 0$ . (Note, such scatter plots as displayed in the figures presented here result from the application of the Monte Carlo method, which yields individual scattering angles and four-momentum components for the scattered particles.)

Upon comparing Figs. 2(a), 3, and 6, we observe the following. For PCS at  $r = r_{\text{mb}}$ , between radially infalling photons ( $E_{\text{ph}} \leq 1$  MeV) and tangentially equatorial orbiting target electrons [Figs. 3(a)–3(e)], the spectrum appears symmetric in  $(P'_{\text{ph}})_r$  for the lowest incident photon energy used:  $E_{\text{ph}} = 0.511$  keV. What role the GM field plays in giving rise to this symmetric distribution is unclear [cf. Fig. 3(a)], since such a distribution is expected in general. In Figs. 3(b)–3(e), for the higher energy incident photons, it appears that GM force component  $(f_{\text{GM}})_r$  of Fig. 2(a) has little effect on the distribution of escaping photons. It seems that the distribution of the scattered photons in the radial direction is, in these cases, dominated by the momentum forces involved in the scattering process itself. That is, as  $E_{\text{ph}}$  is allowed to increase, while  $E_e$  is held constant at 0.539 MeV, the preferred direction of the scattered photon is radially inward—such behavior is to be expected. In addition, even though some of photons are scattered in the positive radial direction, the scattering behavior is inconsistent with what would be expected if  $(f_{\text{GM}})_r$  were important, namely, one would expect for the particles with  $\Theta'_{\text{ph}} \sim \pi/2$ , and large  $(P'_{\text{ph}})_\Phi$ , and thus large  $E'_{\text{ph}}$ , to have positive radial momenta [cf. Figs. 2(a), 3(b)–3(e), 6(b)–6(e), and Eq. (40)].

In the case of PCS by nonequatorially confined target electrons [Figs. 3(f)–3(i), with  $6.145 M^2 m_e^2 \leq Q_e \leq 614.5 M^2 m_e^2$ —i.e., as the energy-momentum of the target particle is allowed to increase, we find that the number of photons with outward radial momenta increases with increasing  $E'_{\text{ph}}$  [implying increasing  $(P'_{\text{ph}})_\Phi$ ]. When one compares the higher energy photons and their polar angles of escape, displayed in Figs. 6(f)–6(i), with Fig. 2(a) and eq. (40), it appears that  $(f_{\text{GM}})_r$  may have some importance in the behavior causing the number of photons scattered with positive radial momenta to increase [cf. Figs. 3(f)–3(i)]. Such behavior could be due, in part, to the fact that  $(f_{\text{GM}})_r$  is large on the particles with large  $(P'_{\text{ph}})_\Phi$  (i.e., large  $E'_{\text{ph}}$ ) and with  $\Theta'_{\text{ph}}$  near  $\sim \pi/2$ ; this is consistent with what we find in the cases of Figs. 3(f)–3(i) and corresponding angles 6(f)–6(i). The other part responsible for the behavior could be that, as  $E_e$  become  $\gg E_{\text{ph}}$ , with increasing  $Q_e$ , backward scattering [ $(P'_{\text{ph}})_r > 0$ ] becomes more effective: cf. 3(d) to 3(f) and 3(g), cf. 3(c) to 3(h) and 3(i), showing progression towards symmetry as  $E_e$  becomes  $\gg E_{\text{ph}}$ . We will return to this discussion after the introduction of Eq. (47).

Before proceeding, note the following: the nonequatorially confined (spherical-like orbiting) target electrons discussed here, and target photons discussed in the next section, for a given distribution, can have either  $P_\Theta < 0$  or  $P_\Theta > 0$ , as the particle passes through the equatorial plane going above or below, respectively. In the figures shown here, one-half of the distribution of 2000 targets are given the negative  $P_\Theta$  value and other half are given the corresponding positive  $P_\Theta$  value (this was not done in [5]). Such a distribution yields what would likely be seen by an observer at infinity. Also, note that, consideration has been given only to collisions between infalling incident particles and bound orbiting target particles, thus, assuming that collisions between neighboring target particles are negligible.

Continuing, now the discussion centers on the various distributions of PCS photons as they escape in the positive and negative  $\hat{e}_\Theta$  directions. Upon comparing Figs. 2(b) and 4–7, we observe that the polar angles  $\Theta'_{\text{ph}}$  of the PCS photons, after scattering off equatorial target electrons [Figs. 6(a)–6(e)] and nonequatorially confined target electrons [Figs. 6(f)–6(i) and 7(a)–7(d)], are consistent with the GM force component  $(f_{\text{GM}})_\Theta$  [Eq. (41)] acting on the scattered particles. The effects can be seen in the polar coordinate momenta  $(P'_{\text{ph}})_\Theta$ , displayed in Figs. 4 and 5—corresponding to cases of Figs. 6 and 7, respectively. Looking closely at the distributions resulting from the equatorial target electrons, the PCS photons go from the general expected symmetric distribution, for the lowest monochromatic incident photon energy used:  $E_{\text{ph}} = 5.11 \times 10^{-4}$  MeV, to being strongly asymmetrical or one-sided, for the highest energy used:  $E_{\text{ph}} = 1$  MeV, with  $E_e = 0.539$  MeV being the same for all the cases; cf. Figs. 4(a)–4(e). Overall, we find that, as the energy of the incident photon  $E_{\text{ph}}$  is increased, more and more of the photons are scattered with  $(P'_{\text{ph}})_r < 0$ ,  $(P'_{\text{ph}})_\Theta > 0$  [i.e., with  $\Theta'_{\text{ph}} > 90^\circ$ ; cf. Figs. 3(a)–3(e), 4(a)–4(e), and 6(a)–6(e)]. Apparent reasons for such distributions are explained in the following.

Recall that the magnitude of the GM potential is  $|\vec{\beta}_{\text{GM}}| = \omega$  (see Section IID). By examining the angle of Eq. (21), we can see how this GM potential, producing the GM tensor field [see Eqs. (37) and (38)], causing the frame dragging,

may alter the incoming angle  $\theta_{\text{ph}}^R$  of the incident photon, and subsequently the outgoing angles,  $\theta_{\text{ph}}^{R'}$  and  $\phi_{\text{ph}}^{R'}$ , of the scattered photon, given by Eq. (22) and Eq. (3.39) of [5]:

$$\phi_{\text{ph}}^{R'} = \phi_{\text{ph}}^R - \arccos \left( \frac{\cos \delta^R - \cos \theta_{\text{ph}}^R \cos \theta_{\text{ph}}^{R'}}{\sin \theta_{\text{ph}}^R \sin \theta_{\text{ph}}^{R'}} \right), \quad (44)$$

respectively, where  $\phi_{\text{ph}}^{R'}$ , the important angle here, gives the direction of the scattered photon, above and below the equatorial plane. [Note, the angles  $\theta_{\text{ph}}^{R'}$  and  $\phi_{\text{ph}}^{R'}$  define the space momentum components as described by a unit four-vector tangent to the coordinate lines at the event  $(r, \Theta, \Phi, t)$ , in the ERF [5]; this particular LNRF coordinate system is centered on the electron with the pole in the direction of positive  $\hat{\mathbf{e}}_{\Phi}$ .] So, in essence, what we are finding is that, the GM force close to event horizon, whose presence is seen by the appearance of the frame dragging velocity  $\omega$  [cf. Eqs. (22) and (44)], exerts a force on the moving particles, causing them to behave in various general relativistic ways (uncharacteristic of Newtonian physics), as discussed further below.

Specifically, for the cases of Figs. 4(a)–4(e), and corresponding Figs. 6(a)–6(e), Eq. (21) shows that  $\theta_{\text{ph}}^R$  will not change for PCS off monochromatic distributions of 2000 target electrons, at  $r_{\text{mb}}$ , if  $E_e (= 0.539 \text{ MeV})$  is held constant for the different cases while  $E_{\text{ph}}$  is allowed to increase, increasing from  $5.11 \times 10^{-4} \text{ MeV}$  to  $1 \text{ MeV}$ . But, increasing  $E_{\text{ph}}$  will, however, change the scattering angle  $\delta^R$ , subsequently, still, altering the scattering angles  $\theta_{\text{ph}}^{R'}$  and  $\phi_{\text{ph}}^{R'}$  [cf. Eqs. (22) and (44)]. So, how does  $\delta^R$  relate to the frame dragging velocity  $\omega$ ? The angle  $\delta^R$  is determined, as stated earlier, from the Klein-Nishina cross section: the effective area of an electron producing a scattering event in which a photon is emitted at particular polar and azimuthal angles,  $\delta^R$  and  $\alpha^R$ , respectively, of a spacetime coordinate system centered on the electron, with the pole in the direction of  $-\hat{\mathbf{e}}_{\mathbf{r}}$  (i.e., of the initial photon direction). The angle  $\delta^R$  depends on the Lorentz factor  $\gamma_e$  of the target electron and the initial incident photon energy  $E_{\text{ph}}$  [see Eq. (20)]. Equation (19) reveals the direct relationship between  $\gamma_e$  and  $\omega$ , and, thus,  $\delta^R$ .

Investigating further, the angle  $\phi_{\text{ph}}^{R'}$ , through the space momentum vector of the scattered photon in the ERF [5]:

$$\begin{aligned} (p_{\text{ph}}^{R'})_r &= p_{\text{ph}}^{R'} \sin \theta_{\text{ph}}^{R'} \cos \phi_{\text{ph}}^{R'}, \\ (p_{\text{ph}}^{R'})_{\Theta} &= p_{\text{ph}}^{R'} \sin \theta_{\text{ph}}^{R'} \sin \phi_{\text{ph}}^{R'}, \\ (p_{\text{ph}}^{R'})_{\Phi} &= p_{\text{ph}}^{R'} \cos \theta_{\text{ph}}^{R'}, \end{aligned} \quad (45)$$

gives, in general, in the four quadrants relative to the equatorial plane, that

$$\begin{aligned} \text{I: } 0 \leq \phi_{\text{ph}}^{R'} \leq 90^\circ, & & \text{II: } 90^\circ \leq \phi_{\text{ph}}^{R'} \leq 180^\circ, \\ (p_{\text{ph}}^{R'})_r \geq 0, & & (p_{\text{ph}}^{R'})_r \leq 0, \\ (p_{\text{ph}}^{R'})_{\Theta} \geq 0, & & (p_{\text{ph}}^{R'})_{\Theta} \geq 0, \\ 90^\circ \leq \Theta'_{\text{ph}} \leq 180^\circ; & & 90^\circ \leq \Theta'_{\text{ph}} \leq 180^\circ; \\ \\ \text{III: } 180^\circ \leq \phi_{\text{ph}}^{R'} \leq 270^\circ, & & \text{IV: } 270^\circ \leq \phi_{\text{ph}}^{R'} \leq 360^\circ, \\ (p_{\text{ph}}^{R'})_r \leq 0, & & (p_{\text{ph}}^{R'})_r \geq 0, \\ (p_{\text{ph}}^{R'})_{\Theta} \leq 0, & & (p_{\text{ph}}^{R'})_{\Theta} \leq 0, \\ 0 \leq \Theta'_{\text{ph}} \leq 90^\circ; & & 0 \leq \Theta'_{\text{ph}} \leq 90^\circ. \end{aligned} \quad (46)$$

We will use the quadrants of Eq.(46), in the discussion below, in an effort to further understand the distribution of PCS photons. (Note, the Lorentz spacetime transformations for eq.(45), from the ERF to a general LNRF observer, are given in [5] [eq. (3.46)]).

Upon comparing Eq. (46) and Figs. 4 and 6, we find the following. In Fig. 4(a) [see also Fig. 3(a)], the photons are scattered symmetrically into the four quadrants. Increasing  $E_{\text{ph}}$  causes the highest energy photons to be scattered below the equatorial plane, and the appearance of a void in the lowest energy regime; cf. Figs. 4(a)–4(e). These figures show how asymmetry in the preferred positive  $\hat{\mathbf{e}}_{\Theta}$  direction, of  $(P'_{\text{ph}})_{\Theta}$ , increases as  $E_{\text{ph}}$  is increased. The highest energy photons are progressively scattered into quadrant II, consistent with  $(f_{\text{GM}})_{\Theta}$  [see Eq. (41) and Fig. 2(b)] acting below the equatorial plane on these scattered particles, proportional to increasing  $(P'_{\text{ph}})_{\Phi}$  (i.e., increasing  $E'_{\text{ph}}$ ), with  $90^\circ \lesssim \Theta'_{\text{ph}} \lesssim 180^\circ$ . On the other hand, the lowest energy photons are progressively scattered into quadrant III, consistent with  $(f_{\text{GM}})_{\Theta}$  acting above the equatorial plane, producing a smaller GM force on these particles, and thus

a smaller magnitude for  $(P'_{\text{ph}})_{\Theta}$ , with  $0 \lesssim \Theta'_{\text{ph}} \lesssim 90^\circ$  [cf. Figs. 6(a)–6(e)]. The most probable explanation for these distributions as related directly to the GM field, although not apparent from Eqs. (40) through (42)—which give the GM force as measured by a LNRF observer, will be given below.

So, overall, the equatorial target electrons scatter the photons preferentially in the direction of positive  $\hat{\mathbf{e}}_{\Theta}$ , as the energy-momentum of the incident photon is increased. The asymmetry seen in the scattered particle distributions described above, at these relatively low incident and target particle energies, while  $E_e (= 0.539 \text{ MeV})$  is held constant, can be viewed as the “signature” of the GM field acting on the infalling  $[(P_{\text{ph}})_r < 0]$  incident photons, and the scattered photons, while increasing  $E_{\text{ph}}$  (i.e., increasing  $|(P_{\text{ph}})_r|$ ). The resulting effects can be seen in the momentum component of Eq. (17), plotted in Figs. 4(a)–4(e), in which the angles contained therein are altered by certain combinations of  $\omega$  and the energy-momenta of the incident and scattered particle energies. The ratio of the number of escaping photons with  $(P'_{\text{ph}})_{\Theta} > 0$  to those with  $(P'_{\text{ph}})_{\Theta} < 0$  ( $\equiv \epsilon_i$ , for particle of type  $i$ ) range from  $\epsilon_{\text{ph}} \simeq 1.07, \simeq 1.46, \simeq 2.42, \simeq 3.42$ , up to  $\simeq 4.99$ , for Figs. 4(a)–4(e), respectively. Thus, as stated earlier, it appears that reflection symmetry of the Kerr metric, above and below the equatorial plane, is broken due to the GM force field.

Note, in general, since  $(P'_{\text{ph}})_{\Phi}$  is positive for all of the escaping Penrose scattered particles, the antisymmetric component  $(f_{\text{GM}})_{\Theta}$  [see Eq. (41) and Fig. 2(b)] will exert a force in the negative  $\hat{\mathbf{e}}_{\Theta}$  direction for  $\Theta'_i < 90^\circ$  and in the positive  $\hat{\mathbf{e}}_{\Theta}$  direction for  $\Theta'_i > 90^\circ$ ; such could aid in the acceleration of the jets of AGNs. Namely, this GM force component has the effect of blueshifting the escaping photons to higher energies, while increasing the Lorentz factor of the escaping electrons.

Now we will consider the PCS by nonequatorially confined target electrons, with the initial monochromatic photon energy held constant at  $E_{\text{ph}} = 5.11 \times 10^{-4} \text{ MeV}$ , while  $E_e$  is allowed to increase from the equatorially confined value  $E_e = 0.539 \text{ MeV}$ ,  $Q_e = 0$  [Fig. 4(a)] up to  $E_e = 5.927 \text{ MeV}$ ,  $Q_e = 154.5 M^2 m_e^2$ , for the different cases [cf.  $(P'_{\text{ph}})_{\Theta}$  and corresponding angles of escape  $\Theta'_{\text{ph}}$  of Figs. 5 and 7, respectively]. The asymmetry proposed to be due to the GM force (indicated by the prominent void) is quite apparent in the different cases [cf. Figs. 5(a)–5(c)], i.e., before, it seems, momentum forces inherent to the scattering processes, because of increasing  $Q_e$ , and the final effects of the GM force acting on the scattered particles, dominate over the initial effects of the GM force, thus, causing symmetry to reappear, as seen in Fig. 5(d). For the nonequatorially confined target electrons, I did not derive expressions as done for the equatorial targets [Eqs. (15) through (22)], showing the direct relationship between the momentum components and the angles producing the asymmetry. Nevertheless, it appears that the asymmetry is caused, in general, by the same mechanism, i.e., the GM force alters the incoming and outgoing angles of Eqs. (22) and (44), through the presence of  $\omega$ . To further compare, the ratio of the number of escaping photons with  $(P'_{\text{ph}})_{\Theta} > 0$  to those with  $(P'_{\text{ph}})_{\Theta} < 0$  range from  $\epsilon_{\text{ph}} \simeq 1.07$  for Fig. 4(a):  $Q_e = 0$  to  $\epsilon_{\text{ph}} \simeq 1.54, \simeq 2.13, \simeq 1.29, \simeq 1.02$ , for Figs. 5(a)–5(d):  $Q_e \neq 0$ , respectively. The specific cause of the behavior for these scattered photon distributions, varying from symmetric to asymmetric [scattering preferentially into quadrants I and II; see Eq. (46)], then back to symmetric (scattering equally into the four quadrants), is not readily accessible from the GM force components [Eqs. (40) through (42)], but, again, the presence of the frame velocity in the scattering angles [Eqs. (22) and (44)] assures us that the GM force field has a role in determining the trajectories of the photons. We will return to these distributions below, where we will find that the asymmetry seen in the scattered particle distributions, at the relatively low incident and target particle energies [Figs. 5(a)–5(c)], while  $E_{\text{ph}} (= 5.11 \times 10^{-4} \text{ MeV})$  is held constant, can be viewed (as in the case of the equatorially confined target electrons described above) as the signature of the GM field acting on the initial infalling photons, and the scattered photons. [Note that, the highest energy photons are scattered with polar escape angles  $\Theta'_{\text{ph}}$  approximately equal to the polar angle indicating the maximum or minimum latitudinal angle of the spherical-like orbiting target electrons ( $\simeq 29.5^\circ$  relative to the equatorial plane), given by Eq. (43); cf. Fig. 7(d).]

Deviating briefly with a discussion to help us to understand better the above scattered particle distributions and those to follow: we do not yet have analytic expressions for the force components [like Eqs. (40) through (42)] describing the behavior of the GM field on a test particle near the event horizon as measured by a “local” BLF  $\overleftrightarrow{\mathbf{H}}$  observer. The reason for this is because of the complexity in deriving an analytic expression for the GM tensor field  $\overleftrightarrow{\mathbf{H}}$  inside the ergosphere in the BLF, i.e., due to the severe dragging of local inertial frames, in which the time coordinate basis vector  $(\partial/\partial t)$  of the Kerr metric changes from timelike to spacelike [7]. Algebraically, this complexity arises in the partial derivatives of the Kerr metric components, contained in the nonzero Christoffel symbols  $\Gamma^k_{ij}$  (sometimes referred to as the affine connections), when evaluating the covariant derivatives in the general expression for  $H_{ij}$  [cf. Eq.(37)]. Therefore, until an exact expression for  $\overleftrightarrow{\mathbf{H}}$  can be found, we can only approximate its physical nature based on the information we have at hand, and what these Penrose scattering processes are telling us, about the behavior of the GM field close to the event horizon. Now, we know that the GM field at radii  $\gg$  than the event horizon ( $r = r_+$ ) appears as a dipolar-like field as measured by a BLF observer. This dipolar-like field will however be distorted near the event horizon as measured by this distant observer, due to large velocities and strong gravity, but not fully destroyed [10]. It is possible that the preference of the particle being scattered into the positive  $\hat{\mathbf{e}}_{\Theta}$

direction is a display of this distorted dipolar-like field. The most probable explanation for the preference in the positive  $\hat{\mathbf{e}}_\Theta$  direction is that, near the event horizon in the BLF, the GM force field lines are frame dragged into the direction of the rotating KBH, i.e., positive azimuthal ( $\hat{\mathbf{e}}_\Phi$ ) direction, which results in  $\overset{\leftrightarrow}{\mathbf{H}}$ , the GM tensor field, acquiring additional cross terms:  $H_{r\Theta}$  and  $H_{\Theta r}$  [cf. Eq. (38)]. This is supported by the acquired nonzero  $\Gamma_{ij}^k$ 's in the covariant derivatives—appearing in the component notation for  $\overset{\leftrightarrow}{\mathbf{H}}$  [see Eq. (37)], which in general gives rise to nonzero  $H_{r\Theta}$  and  $H_{\Theta r}$  components. In this case, the GM vector field, say  $\mathbf{H}$ , will acquire an azimuthal component  $H^\Phi$ , such that  $\mathbf{H} = H^r \hat{\mathbf{e}}_r + H^\Theta \hat{\mathbf{e}}_\Theta + H^\Phi \hat{\mathbf{e}}_\Phi$  [cf. Eq. (39)]. Then, by the analogy of the approximation in the asymptotic rest (or nonrotating) BLF:  $\mathbf{F}_{\text{GM}} \simeq \mathbf{P} \times \mathbf{H}$ , for  $r \gg r_+$ , and using Eq. (37), we find that the GM force on a test particle as measured by a local BLF (LBLF) observer, for  $r \sim r_+$ , can be expressed by the following:

$$\begin{aligned} \mathbf{F}_{\text{GM}} &= \overset{\leftrightarrow}{\mathbf{H}} \cdot \mathbf{P} \\ &= [(F_{\text{GM}})_{r\Theta}, (F_{\text{GM}})_{\Theta r}, (F_{\text{GM}})_{\Phi}] \\ &= (H_{r\Theta} P^\Theta + H_{r\Phi} P^\Phi) \hat{\mathbf{e}}_r + (H_{\Theta r} P^r + H_{\Theta\Phi} P^\Phi) \hat{\mathbf{e}}_\Theta + (H_{\Phi r} P^r + H_{\Phi\Theta} P^\Theta) \hat{\mathbf{e}}_\Phi \\ &\approx (H^\Phi P_\Theta - \tilde{H}^\Theta P_\Phi) \hat{\mathbf{e}}_r + (H^r P_\Phi - \tilde{H}^\Phi P_r) \hat{\mathbf{e}}_\Theta + (H^\Theta P_r - \tilde{H}^r P_\Theta) \hat{\mathbf{e}}_\Phi \end{aligned} \quad (47)$$

[ $\approx$  indicates the omission (for our analyzing purposes) of the space diagonal Kerr metric tensor components  $g^{jk}$ , multiplying the covariant momentum components]. The components of the vectors  $\mathbf{H}$  and  $\tilde{\mathbf{H}}$  are defined by the components of the GM tensor:

$$\begin{aligned} H^r &\equiv H_{\Theta\Phi}, & \tilde{H}^r &\equiv -H_{\Phi\Theta}, \\ H^\Theta &\equiv H_{\Phi r}, & \tilde{H}^\Theta &\equiv -H_{r\Phi}, \\ H^\Phi &\equiv H_{r\Theta}, & \tilde{H}^\Phi &\equiv -H_{\Theta r} \end{aligned} \quad (48)$$

[cf. Eqs. (38), (39), and (40) through (42)]. If the GM tensor is antisymmetric [see Eq. (39)], then  $H^r = \tilde{H}^r$ ,  $H^\Theta = \tilde{H}^\Theta$ ,  $H^\Phi = \tilde{H}^\Phi$ .

From a geometrical analysis of the characteristics of the antisymmetric GM tensor components  $\overset{\leftrightarrow}{\mathbf{H}}$  in the asymptotic rest BLF (ABLF) [see Eq. (39)] and the components of  $\overset{\leftrightarrow}{\mathbf{H}}$  in the LNRf in which the frame dragging is “taken out” [see Eq. (38)], and the probable condition in the LBLF, that the GM tensor field lines are frame dragged in the azimuthal direction, we can deduce that the GM tensor in the LBLF will be somewhat similar to that in the LNRf, in respect to the dipolar-like characteristics, with differences, in general, depending on the frame dragging velocity  $\omega$  [cf. Eq. (37)]. The tensor components of Eq. (38), when evaluated at  $r \sim r_+$ , reveal to us the following:

$$\begin{aligned} H^r &\leq 0 \text{ and } \tilde{H}^r \leq 0 \text{ for } \Theta \leq 90^\circ; \\ H^r &\geq 0 \text{ and } \tilde{H}^r \geq 0 \text{ for } \Theta \geq 90^\circ; \\ H^\Theta &> 0 \text{ for } \Theta \leq 90^\circ \text{ and } \Theta > 90^\circ; \\ \tilde{H}^\Theta &< 0 \text{ for } \Theta \leq 90^\circ \text{ and } \Theta > 90^\circ; \\ H^\Phi &< 0 \text{ for } \Theta \leq 90^\circ \text{ and } \Theta > 90^\circ; \\ \tilde{H}^\Phi &> 0 \text{ for } \Theta \leq 90^\circ \text{ and } \Theta > 90^\circ; \end{aligned} \quad (49)$$

cf. Eqs. (47) and (48). The additional components included in Eq. (49),  $H^\Phi$  and  $\tilde{H}^\Phi$ , are found from deductive reasoning as follows. We know from a general direct evaluation of the covariant derivative of  $\vec{\beta}_{\text{GM}}$  that  $H_{r\Theta} = H_{\Theta r}$ . Therefore assuming that  $H_{r\Theta} = H_{\Theta r} > 0$  (as would be expected because of the frame dragging), then by definition [Eq. (48)] and the results of the Penrose scattered particle distributions, we can deduce the general signs of  $H^\Phi$  and  $\tilde{H}^\Phi$  in, above, and below the equatorial plane. We will use the relations of Eq. (49), as we continue in the discussion below.

Note, the differences between the three frames of reference considered here are the following. An observer in the BLF measures coordinates  $r$ ,  $\Theta$ ,  $\Phi$ , and  $t$ , relative to the KBH. The BLF is an inertial frame. An observer in this frame measures spacetime events from two points of view: the asymptotic rest (or flat) inertial frame (events occurring at  $r \gg r_+$ )—which I refer to as the ABLF, and the local inertial frame (events occurring at  $r \sim r_+$ )—which I refer to as the LBLF. The measured four-momenta [ $P_\mu = (P_r, P_\Theta, L, -E)$ ], describing the trajectories of the particles [cf. Eqs. (12) through (14)], are the same for both these BLF observers, although the immediate surroundings of the particles are very different. The LBLF observer measures the effects of frame dragging, whereas the ABLF does not, yet both observers are located at infinity. For example, the GM tensor field as measured by the ABLF observer will have prominent dipolar-like features [cf. (39)], features that will be distorted as measured by the LBLF observer. An

observer in the LBLF “sees” this distorted field, whose force lines are frame dragged into the azimuthal direction, and measures its effects on moving test particles [cf. Eq. (47)], but the ABLF observer cannot measure these local effects; it is only through the “eyes” of the LBLF observer, as evident in these Penrose process distributions, that the observer at infinity can measure these local effects. Now, on the other hand, the LNRF observer is a local inertial frame rotating with the geometry [7], experiencing in a sense no frame dragging. This spacetime coordinate system is at rest relative to the frame dragging, and revolves with velocity  $\omega$  relative to the observer at infinity. Physical processes described in this local Lorentz frame are “simpler” because the frame dragging is canceled as much as possible. The observer in the LNRF measures the force that the local gravitationally distorted dipolar-like GM tensor field exerts on a moving test particle, however, free of frame dragging effects. Therefore, the LNRF has its limitations in explaining the local effects of the frame dragged GM force field; for this reason, the LBLF is needed (which, by definition, can also be referred to as just the BLF).

Equation (47) shows that the GM force on a test particle in the LBLF (wherein we are assuming the most probable condition) will acquire additional terms in the radial and polar components, different from that in the ABLF and the LNRF. [Note, in the LNRF, Eqs. (40) through (42) have the same general form as Eq. (47), however, with  $H^\Phi = \tilde{H}^\Phi = 0$ .] These additional terms involving  $H^\Phi$  and  $\tilde{H}^\Phi$ , as we shall see, can explain the asymmetries that we observe in the Penrose scattered particle distributions presented here. For a preliminary example, if  $P_r$  is less than zero, and allowed to increase in magnitude for the different cases considered, as for the initial radially infalling photon [ $(P_{\text{ph}})_r < 0$ ,  $(P_{\text{ph}})_\Theta = (P_{\text{ph}})_\Phi = 0$ ] displayed in Figs. 3(a)–3(e); 4(a)–4(e); 6(a)–6(e), with the target particle having relatively low energy-momentum, Eq. (47) shows that  $(F_{\text{GM}})_\Theta$  will exert a dominant force on the photon, increasing in the positive  $\hat{e}_\Theta$  direction, and thus, initializing the asymmetry eventually seen in the high energy PCS photons [cf. Figs. 4(a)–4(e) and 6(a)–6(e)]. Now, with this initialized asymmetry, the final distributions are consistent with  $(F_{\text{GM}})_\Theta$ , again as given by Eq. (47), acting directly on the PCS photons: In addition to this force component being positive for photons scattered with  $(P'_{\text{ph}})_r < 0$  and  $H^r \geq 0$  [i.e.,  $\Theta'_{\text{ph}} \geq 90^\circ$ ; cf. Eq. (49)], this force component will be positive for photons scattered with  $(P'_{\text{ph}})_r > 0$  and  $H^r > 0$  [i.e.,  $\Theta'_{\text{ph}} > 90^\circ$ ] provided  $H^r (P'_{\text{ph}})_\Phi > \tilde{H}^\Phi (P'_{\text{ph}})_r$ , as for the photons with large  $L'_{\text{ph}}$  or small  $(P'_{\text{ph}})_r$ —otherwise this force component will be negative. For  $(P'_{\text{ph}})_r < 0$  and  $H^r < 0$  (i.e.,  $\Theta'_{\text{ph}} < 90^\circ$ ),  $(F_{\text{GM}})_\Theta$  will be  $> 0$  for sufficiently small  $L'_{\text{ph}}$  or sufficiently large  $|(P'_{\text{ph}})_r|$ —otherwise  $(F_{\text{GM}})_\Theta$  will be  $< 0$ . This behavior is consistent with Figs. 4(a)–4(e). On the other hand, if the energy-momentum of the infalling incident photon is relatively small compared to that of the orbiting target electron [in which, say  $(P_e)_\Phi$  is allowed to increase for different cases, with  $(P_e)_r = 0$ ], Eq. (47) shows that  $(F_{\text{GM}})_\Theta$ , exerted on the scattered photon, will dominate, creating or recreating symmetry in the polar direction. We find this behavior to be consistent with what we observe in the PCS photons of Figs. 4(a), 5, 6(a), 7. More on this later.

So, in general, Eq. (47) shows that it is the  $\tilde{H}^\Phi$  component of the GM tensor field in the LBLF, acting on radial component of the infalling incident particles, that subsequently causes the polar angle  $\Theta'_i$ , of the scattered particles of type  $i$ , to be  $> 90^\circ$  (i.e.,  $P'_\Theta > 0$ ). Once the preference of the scattering angle  $\Theta'_i > 90^\circ$  has been established by the GM force as measured by a LBLF observer, we find that the scattered particle trajectories are somewhat consistent with the GM force as measured by a LNRF observer [Eqs. (40) through (42)]—however, the trajectories cannot be fully explained in this frame. Therefore, in the remainder of this discussion, we will now use Eq. (47), the proposed, most probable GM force measured by a LBLF observer, which includes the use of Eqs. (40) through (42) as measured by a LNRF observer, to further show the effects that the GM field has on these Penrose scattering processes—remembering that the BLF observer, i.e., the observer located at infinity measures both local events ( $r \sim r_+ \equiv \text{LBLF}$ ) and faraway events ( $r \gg r_+ \equiv \text{ABLF}$ ).

Before proceeding, we return to the cases of Fig. 5 to shed some additional light on these distributions using Eq. (47). The radial distributions of these PCS photons remain nearly symmetrical for the different cases (not displayed here), looking very much like the case of Fig. 3(a), where there is a slight preference for the number of particles escaping with  $(P'_{\text{ph}})_r < 0$ . Using Eq. (49), Eq. (47) shows in general that for  $H^r \geq 0$  (i.e.,  $\Theta_i \geq 90^\circ$ ) and  $P_r < 0$ ,  $(F_{\text{GM}})_\Theta$  is  $> 0$ . But for  $P_r > 0$  and  $H^r > 0$  (i.e.,  $\Theta_i > 90^\circ$ ),  $(F_{\text{GM}})_\Theta$  is  $> 0$  or  $< 0$  for sufficiently large or small azimuthal momentum  $P_\Phi (= L)$ , respectively. On the other hand, Eq. (47) shows in general that for  $H^r \leq 0$  (i.e.,  $\Theta_i \leq 90^\circ$ ) and  $P_r > 0$ ,  $(F_{\text{GM}})_\Theta$  is  $< 0$ . But for  $P_r < 0$  and  $H^r < 0$  (i.e.,  $\Theta_i < 90^\circ$ ),  $(F_{\text{GM}})_\Theta$  is  $< 0$  or  $> 0$  for sufficiently large or small azimuthal momentum  $P_\Phi$ , respectively. Thus, the above analysis shows possible symmetry in the polar direction if there is symmetry in  $P'_r$  of the scattered particles distribution. However, if there is asymmetry in  $P'_r$ , say, the particles are scattered preferentially with  $P'_r < 0$ , there will be asymmetry in the polar direction: For  $P'_r < 0$ , the component  $(F_{\text{GM}})_\Theta$  acting on the particles with  $\Theta'_i \geq 90^\circ$  will be  $> 0$ , but  $(F_{\text{GM}})_\Theta$  acting on particles with  $\Theta'_i < 90^\circ$  will be  $> 0$  for particles with  $|H^r P'_\Phi| < |\tilde{H}^\Phi P'_r|$  (implying small  $L'$ , low  $E'$  or large  $|P'_r|$ ) and  $< 0$  for particles with  $|H^r P'_\Phi| > |\tilde{H}^\Phi P'_r|$  (implying large  $L'$ , high  $E'$  or small  $|P'_r|$ ). This behavior of Eq. (47) is sufficient to give a general explanation for the polar asymmetries occurring in these Penrose scattering processes if there is asymmetry in the scattered particle spectral distribution of  $P'_r$  [cf. Figs. 3(a)–3(e) and 4(a)–4(e)]. Yet, if there is symmetry in  $P'_r$  [or

near symmetry—as we find for the cases of Figs. 5], Eq. (47) shows that  $(F_{\text{GM}})_{\Theta}$  acting on the scattered particles should produce symmetry in the polar direction. However, because of the initial asymmetry, favoring the positive  $\hat{\mathbf{e}}_{\Theta}$  direction, caused by the GM force component  $(F_{\text{GM}})_{\Theta}$  acting on the radial component  $(P_{\text{ph}})_r$  of the infalling incident photons [cf. Eq. (47)], the scattered particle distributions, at sufficiently low orbital energy-momentum for the target particle, will not reflect the expected mirror symmetry, above and below the equatorial plane—contrary to what one would expect in Newtonian physics or in the weak gravitational regime ( $r \gg r_+$ ); this can be seen in Figs. 5(a)–5(c). That is, according to the first term in  $(F_{\text{GM}})_{\Theta}$  [cf. Eq. (47)] and the description above for small  $L'$  (or for the satisfying of  $|H^r P'_{\Phi}| < |\tilde{H}^{\Phi} P'_r|$ ), this initial asymmetry in the  $+\hat{\mathbf{e}}_{\Theta}$  direction is amplified when  $(F_{\text{GM}})_{\Theta}$  acts on the subsequent PCS photons. But, as  $Q_e$  of the nonequatorially confined target electrons is allowed to increase for the different cases, i.e., increasing the magnitudes of  $(P_e)_{\Theta}$  and  $L_e$ , and subsequently  $(P'_{\text{ph}})_{\Phi}$ , the first term in  $(F_{\text{GM}})_{\Theta}$  dominates over this initial asymmetry, causing the reappearance of the symmetry we observed in Fig. 5(d), thus, showing us the final result of  $(F_{\text{GM}})_{\Theta}$  acting on the scattered high energy photons, increasing in magnitude with increasing  $L'_{\text{ph}}$ . So, in essence,  $(F_{\text{GM}})_{\Theta}$  gives the escaping particles with large azimuthal component momentum a boost into opposite polar directions, and is greater in the  $+\hat{\mathbf{e}}_{\Theta}$  direction for particles with  $(P'_{\text{ph}})_r < 0$  [cf. Figs. 3(a)–3(e) and 4(a)–4(e)].

Now proceeding with the discussion after the brief deviation, the momenta  $(P'_{\text{ph}})_{\Theta}$  of Figures 4(f)–4(i), from PCS of 2000 radially infalling photons (for each case) by nonequatorially confined target electrons, show presence of the GM force acting on the particles. Effects of  $(F_{\text{GM}})_{\Theta}$  [of Eq. (47)] acting on  $(P_{\text{ph}})_r$  of the initial photons,  $E_{\text{ph}} = 0.15$  MeV [Figs. 4(f), 4(g)] and  $E_{\text{ph}} = 0.03$  MeV [Figs. 4(h), 4(i)], can clearly be seen, by the presence of the most prominent regions void of particles [cf. Figs. 4(d) and 4(e)]. This feature (viewed as the signature of the GM field acting on the infalling incident photons, and the scattered photons) is somewhat permanent at these initial energies, in the sense that  $(F_{\text{GM}})_{\Theta}$  acting on the PCS photons resulting from the target nonequatorially confined electrons, of initial energy  $E_e \simeq 1.297$  MeV,  $E_e = 5.927$  MeV, and  $E_e = 11.79$  MeV [Figs. 4(f)–4(i)], the “symmetry producing agent,” will not dominate over the effects producing this feature [as in Fig. 5(d)]. Once the preference for  $\Theta'_{\text{ph}} > 90^\circ$  has been established by  $(F_{\text{GM}})_{\Theta}$  acting on the infalling incident photons, as described above, the additional asymmetry seen in Figs. 4(f)–4(i) is consistent with  $(F_{\text{GM}})_{\Theta}$  acting on the escaping photons, which are scattered predominantly with  $(P'_{\text{ph}})_r < 0$  [see Figs. 3(f)–3(i)]. According to Eq. (47), for  $(P'_{\text{ph}})_r < 0$ ,  $(F_{\text{GM}})_{\Theta}$  will be  $> 0$  (or in the  $+\hat{\mathbf{e}}_{\Theta}$  direction) for all the photons scattered with  $\Theta'_{\text{ph}} \geq 90^\circ$ , but those with  $\Theta'_{\text{ph}} < 90^\circ$ ,  $(F_{\text{GM}})_{\Theta}$  will be  $> 0$  if  $|H^r L'_{\text{ph}}| < |\tilde{H}^{\Phi} (P'_{\text{ph}})_r|$ , as for the lowest energy PCS photons; otherwise  $(F_{\text{GM}})_{\Theta}$  will be  $< 0$ , i.e., for photons scattered with sufficiently larger energies. This is the behavior we observe in Figs. 4(f)–4(i) [cf. also corresponding escape angles of Figs. 6(f)–6(i), respectively]. For example, notice how  $(F_{\text{GM}})_{\Theta}$  acting on the PCS photons resulting from the nonequatorially confined target electrons (the symmetry producing agent) of increasing orbital energy-momentum, for the different cases, causes more and more high energy PCS photons to be emitted in the negative  $\hat{\mathbf{e}}_{\Theta}$  direction, and, thus, eventually causes symmetry to somewhat reappear except for the GM signature [cf. Figs. 4(h) and 4(i) to 5(d)]. Moreover, according to Eq. (47), as  $E_e$  increases and more and more of the photons are scattered with  $(P'_{\text{ph}})_r > 0$ , for  $\Theta'_{\text{ph}} \leq 90^\circ$ ,  $(F_{\text{GM}})_{\Theta}$  will be  $< 0$ , assisting in reestablishing the symmetry [cf. Figs. 3(f)–3(i)]. Note, the ratio of the number of escaping photons with  $(P'_{\text{ph}})_{\Theta} > 0$  to those with  $(P'_{\text{ph}})_{\Theta} < 0$ ,  $\epsilon_{\text{ph}}$ , range from  $\simeq 2.41$  for Fig. 4(f) to  $\simeq 1.34$ ,  $\simeq 1.16$ , and  $\simeq 1.08$  for Figs. 4(g)–4(i), respectively.

Astrophysically, these results mean that an observer at infinity will observe “photon jets,” collimated concentric the polar axis, ranging from symmetric to asymmetric, depending on the accretion disk properties: which populate the target particle orbits and supply the infalling incident photons. So, overall, in summary, it appears that the angle  $\phi_{\text{ph}}^R$ , measured perpendicular to the equatorial plane, in the ERF (a particular LNRF observer), given by Eq. (44), is altered by the presence of  $\omega$ , the frame dragging velocity, such that certain combinations of increasing  $E_{\text{ph}}$  and/or  $E_e$  (i.e., increasing the energy-momenta of the incident and target particles) cause the scattered particle distributions to vary from symmetric to asymmetric, with the preference in the direction of positive  $\hat{\mathbf{e}}_{\Theta}$ , then back to very nearly symmetric. The behavior of these distributions is in some degree consistent with the GM force as measured by a LNRF observer [Eqs. (40) through (42)], but this behavior cannot be fully explained in this frame. The most probable explanation, that near the event horizon the GM field lines are frame dragged in the  $+\hat{\mathbf{e}}_{\Phi}$  direction as measured by a local frame dragged inertial observer [leading to the derivation of the general expression Eq. (47) for the GM force as measured locally (at  $r \sim r_+$ ) by a BLF observer], can indeed explain this behavior. We shall find this to be true also for the PPP discussed below.

## B. The Gravitomagnetic Field and PPP ( $\gamma\gamma \rightarrow e^-e^+$ )

Now considering the PPP ( $\gamma\gamma \rightarrow e^-e^+$ ), displayed in Figs. 8 and 9 are scatter plots of  $(P_{\mp})_{\Theta}$  [Eq. (26)] and the corresponding polar angles  $\Theta_{\mp}$  [Eq. (43)], respectively, of the escaping  $e^-e^+$  pairs for various cases, after 2000 PPP

events at the photon orbit for each case. In general, the force component  $(F_{\text{GM}})_{\Theta}$  of Eq. (47), using Eq. (49), reveals to us that infalling particles ( $P_r < 0$ ) and outgoing particles ( $P_r > 0$ ) moving along the equatorial plane ( $\Theta_i = 90^\circ$ ) will experience a force  $(F_{\text{GM}})_{\Theta} > 0$  and  $(F_{\text{GM}})_{\Theta} < 0$ , respectively. The GM force component  $(F_{\text{GM}})_{\Theta} > 0$  acting on the infalling incident photon of energy  $E_{\gamma 1} = 0.03$  MeV is expected to be somewhat significant in initializing the asymmetry, above and below the equatorial plane, favoring the positive  $\hat{\mathbf{e}}_{\Theta}$  direction ( $\Theta_i > 90^\circ$ ), eventually seen in the scattered particle distributions, in the relatively low energy regime, as indicated in Fig. 4(c). However, this asymmetry is not apparent in the case of Figs. 8(a) and 9(a). In this case it appears that, this initialized asymmetry is balanced (or canceled) by  $(F_{\text{GM}})_{\Theta}$  acting on the outgoing  $e^-e^+$  pairs—at these relatively low incident and target particle energies ( $E_{\gamma 2} = 13.54$  MeV), where for  $\Theta_{\mp} \leq 90^\circ$ , and if the condition is satisfied that  $|H^r L_{\mp}| < |\tilde{H}^{\Phi}(P_{\mp})_r|$  for  $\Theta_{\mp} > 90^\circ$ ,  $(F_{\text{GM}})_{\Theta}$  will be in the negative  $\hat{\mathbf{e}}_{\Theta}$  direction: Such could very well balance or cancel out the effects of  $(F_{\text{GM}})_{\Theta} > 0$  acting on the initial infalling incident photons. Note that, the only PPP electrons satisfying the escape conditions are those with  $(P_{\mp})_r > 0$ ; electrons with  $(P_{\mp})_r < 0$  fall into the black hole since the PPP ( $\gamma\gamma \rightarrow e^-e^+$ ) takes place at the photon orbit [5]. Now, on the other hand, at larger energies, as in the cases of Figs. 8(b)–8(d) and 9(b)–9(d), the initialized asymmetry, produced by  $(F_{\text{GM}})_{\Theta}$  acting on  $(P_{\gamma 1})_r < 0$  (of the infalling incident photon), becomes less and less balanced as  $L_{\mp}$  increases (implying increasing  $E_{\mp}$ ), as the condition  $|H^r L_{\mp}| > |\tilde{H}^{\Phi}(P_{\mp})_r|$  becomes satisfied, at which  $(F_{\text{GM}})_{\Theta}$  behaves like an antisymmetric function about the equatorial plane, with  $(F_{\text{GM}})_{\Theta} < 0$  for  $\Theta_{\mp} \leq 90^\circ$  and  $(F_{\text{GM}})_{\Theta} > 0$  for  $\Theta_{\mp} > 90^\circ$ , for  $(P_{\mp})_r > 0$ , superimposed with the established initial preference for  $\Theta_{\mp} > 90^\circ$ . So, underlining the cause of the symmetry and asymmetry we observe in Figs. 8 and 9, in general, is a tug-of-war between the dominance of the symmetry producing term  $H^r L_{\mp}$  [reflecting momentum transferred from the initial conditions  $L_{\gamma 2}$ ,  $(P_{\gamma 2})_{\Theta}$ ] and the asymmetry producing term  $\tilde{H}^{\Phi}(P_{\gamma 1})_r$ ; more on this below. Note, like the PCS, the way in which the GM field acts directly on the particles in these PPP ( $\gamma\gamma \rightarrow e^-e^+$ ) processes, wherein we do not have to apply Eq. (47) manually as in these analyses, is through the presence of  $\omega$ , the frame dragging velocity [cf. Eqs. (24) through (30)], related to GM potential (see Section IID), contained in the Kerr metric [Eq. (1)]: The Kerr metric defines the paths of spacetime trajectories of particles interacting and “flowing” along geodesics, with four-momenta  $P_{\mu} = (P_r, P_{\Theta}, L, -E)$ , in the gravitational field (or curved spacetime) of a rotating black hole, as measured by an observer at infinity.

Looking further at the different cases in Figs. 8 and 9, for the case of Figs. 8(a) and 9(a) it appears that  $(F_{\text{GM}})_{\Theta}$  [Eq. (47)] is somewhat balanced, as described above, in such a way that the final result is a nearly symmetric distribution—like that expected from a Newtonian point of view—with the ratio  $\epsilon_{\mp} \simeq 1.12$  (defining the number of  $e^-e^+$  pairs scattered below to those scattered above the equatorial plane). In the cases of Figs. 8(b) to 8(d) the ratio  $\epsilon_{\mp} \simeq 1.74, \simeq 2.51, \simeq 2.61$ , respectively. Thus, in light of the general conclusion above, the distributions of Figs. 8(b) to 8(d) are consistent with both terms in  $(F_{\text{GM}})_{\Theta}$  [Eq. (47)] being significant: the first term gives the high energy PPP electrons a boost into opposite polar directions [cf. Fig. 1(a)]; the second term acting in dominance on the incident infalling photons after the PPP electrons satisfy the condition  $|H^r L_{\mp}| > |\tilde{H}^{\Phi}(P_{\mp})_r|$ , provides the asymmetry, favoring the positive  $\hat{\mathbf{e}}_{\Theta}$  direction.

Overall, in these PPP ( $\gamma\gamma \rightarrow e^-e^+$ ) processes, we find that the intrinsic “ $e^-e^+$  jet” (positive  $\hat{\mathbf{e}}_{\Theta}$  direction) to counter jet (negative  $\hat{\mathbf{e}}_{\Theta}$  direction) asymmetry (defined by  $\epsilon_{\mp}$ ) increases, first quickly, as above (cf. Fig. 8), then slowly, to a ratio of  $\simeq 3 : 1$ , for the maximum energy that can be used for the target photon in these processes,  $E_{\gamma 2} \sim 108$  GeV (i.e., before the computer simulation breaks down; see [5] for detailed construction of computer codes). Astrophysically, what this means is that as  $E_{\gamma 2}$  is increased, implying increasing the energy-momentum of the escaping PPP electrons, the luminosities in the jet ( $L_{\text{Jet}}$ ) and counter jet ( $L_{\text{CJet}}$ ) get more one-sided, mimicking the effects associated with relativistic beaming, until a maximum ratio in luminosity ( $\simeq 3 : 1$ ) is reached. We see this occurring when we let these PPP electrons undergo “secondary” PCS with infalling disk photons [25], allowing us to obtain  $\gamma$ -ray luminosities. It is presumed that such a  $\simeq 3 : 1$  ratio in jet luminosities would also exist in synchrotron radiation if the PPP electrons were allowed to interact with a surrounding magnetic field. Thus, it appears that relativistic beaming near line of sight of the observer, in general, will be needed to explain observations if the observed  $L_{\text{Jet}}/L_{\text{CJet}}$ , in a source powered by a black hole, is greater than  $\sim 3$  for the high energy  $\gamma$ -ray or synchrotron emission. Nevertheless, importantly, these Penrose processes acting in conjunction with the GM field can serve the purpose of beaming the escaping particles into the polar direction, probably creating the initial jets of AGN. The intrinsic magnetic field produced by the dynamo-like action associated with the swirling (vortical orbiting [26]) escaping Penrose produced highly relativistic plasma, about the polar axis, may be important also, at least in the observed synchrotron emission of the jets, and perhaps in maintaining collimation: this statement must be investigated further.

In addition, when analyzing the GM radial component  $(F_{\text{GM}})_r$  of Eq. (47), using Eqs. (49), (40), and Fig. 2(a), to see what effects this component has on the PPP electrons, we get the following. For  $e^-e^+$  pairs scattered with  $(P_{\mp})_{\Theta} \leq 0$ ,  $(F_{\text{GM}})_r > 0$  [cf. Fig. 2(a)]. But for  $(P_{\mp})_{\Theta} > 0$ ,  $(F_{\text{GM}})_r > 0$  for  $|H^{\Phi}(P_{\mp})_{\Theta}| < |H^{\Theta}(P_{\mp})_{\Phi}|$ —as would be for the higher energy particles; otherwise  $(F_{\text{GM}})_r < 0$ —as would be for the lower energy particles or particles with large

$(P_{\mp})_{\Theta} > 0$ . Since in this case, only the PPP electrons with  $(P_{\mp})_r > 0$  escape (on the average one of the pairs escapes, while the other falls into the black hole [5]), it is not clear what role the radial component of the GM force plays. However, looking back at the radial spectra of the PCS photons, this behavior appears to be a contributing factor to the progressive asymmetry of  $(P'_{\text{ph}})_r$  seen in the escaping photons with large  $(P'_{\text{ph}})_{\Theta} > 0$  after being scattered by equatorially confined target electrons [cf. Figs. 3(a)–3(e) and 4(a)–4(e)]; and the reestablishing the symmetry seen in  $(P'_{\text{ph}})_r$  for the high energy particles [implying large  $(P'_{\text{ph}})_{\Phi}$ ] after being scattered by the nonequatorially confined target electrons [cf. Figs. 3(f)–3(i) and 4(f)–4(i)].

So, overall, for the PCS and the PPP ( $\gamma\gamma \rightarrow e^-e^+$ ) considered here, in general, the asymmetries seen in the scattered particle distributions, above and below the equatorial plane, that one would, in nonrotating space (or pseudo flat space), expect to be symmetrical, can be attributed to the GM field acting on the incident and scattered particles. Specifically, it is a tug-of-war between conditions  $|H^r P_{\Phi}| \lesseqgtr |\tilde{H}^{\Phi} P_r|$  defined by Eq. (47) that causes the asymmetry, which varies through a ratio of  $\sim 3 : 1$  in the  $e^-e^+$  jet to counter jet for PPP ( $\gamma\gamma \rightarrow e^-e^+$ ), and a ratio of  $\sim 5 : 1$  in the photon jet to counter jet for PCS. Thus, the GM force, more or less, breaks the expected reflection symmetry, above and below the equatorial plane. These Penrose processes, which occur near the event horizon, allow us to see this general relativistic effect in action.

#### IV. CONCLUSIONS

It has been shown in this investigation that Penrose scattering processes in the ergosphere of a KBH can produce x-ray,  $\gamma$ -ray, and  $e^-e^+$  pair energies comparable to those observed in quasars and other AGNs. This model can work for any size accretion disk (thin or “thick”) and any size black hole. It has been shown also that the asymmetry in the distribution of Penrose scattered particles, above and below the equatorial plane, can be attributed to the GM field—the gravitational force field produced by the angular momentum of the KBH, which causes local inertial frames to be dragged into the direction that the black hole is rotating (sometimes called the Lense-Thirring effect). It has become apparent through these Penrose processes that the GM force field lines, inside the ergosphere, close to the event horizon, are frame dragged into the positive azimuthal direction in the local frame of the observer at infinity, resulting in particle distributions appearing to break the expected reflection symmetry of the Kerr metric (which describes the geometry outside of a rotating black hole) above and below the equatorial plane.

Overall, these model calculations strongly suggest that the momenta of the Penrose scattered particles naturally aid in the production of one-sided and two-sided polar jets, consistent with the jets associated with AGNs. Moreover, the variations between symmetry and asymmetry found in the scattered particle distributions, and thus in densities, due to the GM field acting on the space momenta of the incoming, outgoing particles, could contribute to the overall individual “blob-like” structures we observe in the jets of AGNs; this should, however, be investigated further.

Importantly, we have the following conclusion from this investigation: The astrophysical conceptual fact is that rapidly rotating black holes give rise to Penrose processes and strong GM forces, which in turn produce high energy particle jets with symmetrical and asymmetrical distributions: differing by a factor as high as  $\sim 3 - 5$ , above and below the equatorial plane. This must be taking into account in AGN models when applying relativistic beaming effects [27,28,29,30].

In addition, this investigation suggests an answer to the long asked question concerning whether or not the asymmetry in the jet and counter jet distributions is intrinsic to the energy source [31]. The suggested answer, in general, is yes, although Doppler boosting due to relativistic beaming [32,33] when the emission axis of the jet is near the line of sight of the observer, may still in some cases serve as an important enhancement mechanism, to increase the apparent observed luminosities and energies, particularly when superluminal motion in the jet flow is apparent and/or the jet and counter jet luminosities differ by more than a factor  $\sim 3 - 5$ . Details of how these Penrose scattering processes relate to AGNs, their observed luminosities, and relativistic beaming models, are discussed in other papers by the author [25,34].

Further, the model presented here to extract energy-momentum from a rotating black hole by Penrose escaping particles, along with the intrinsic magnetic field associated with this relativistic vortical orbiting escaping “plasma,” which is expected to give rise to synchrotron radiation—being consistent with observations, suggests a complete, self-consistent model, without the necessity of the external magnetic field of the accretion disk. The attempted use of the external magnetic field of the accretion disk in a dominant role to extract rotational energy from a black hole, by having the magnetic field lines torque the horizon and/or the accretion material near the horizon (i.e., the Blandford-Znajek (BZ) type models; see [35] and references therein), introduces historical problems yet to be solved, namely, how to convert from electromagnetic energy to relativistic particle energy, such that particles are ejected along field lines into the polar direction: and related problems, such as how to keep the field lines from becoming tangled (or to be sufficiently tangled); how to generate the large magnetic field strengths needed (1) if the relativistic

particles are to be created along the field lines and (2) to be consistent with the most luminous AGNs; and of course the causality problem—for models assuming the magnetic field lines are “anchored” to the horizon; see [36]. However, the electromagnetic field of the accretion disk could, perhaps, play an important role on a large scale in assisting the jets of the Penrose escaping particles, in further collimation and acceleration, out to the observed kiloparsec distances of AGN jets. The large scale magnetic field of the accretion disk may also be important in transporting angular momentum outward enabling material to be accreted into the black hole [37]. By the same token, since the GM field provides a way through these Penrose processes to transport angular momentum from particles inside the ergosphere, outward to infinity, it may also provide a way to transport angular momentum outward, in the “static” [7] accretion disk regime ( $r > 2M$ , i.e., where the severe frame dragging is less): This statement seems worthy of an investigation.

In addition, the Penrose process distributions described here, of escaping particles, are consistent with the disk returning photons [38], gravitationally focused after being emitted from radii  $< r_{\text{ms}} (\simeq 1.2M)$ , the marginally stable orbit. As measured by an observer at infinity, the PCS photons are reemitted with the highest energy photons scattered along geodesics concentrated in the equatorial plane. Notice, the cases of Figs. 3(b), 6(b) and 3(a), 6(a), 7(a)-7(c) can be used to explain the observations of the classical stellar/galactic black-hole candidate Cygnus X-1 [39] and the broad Fe  $K\alpha$  emission line at  $\sim 6$  keV, with the associated reflection (“backscattered”) continuum, of the bright Seyfert 1 galaxy (AGN) MCG—6-30-15 [35], respectively. The case similar to that of Figs. 3(b) and 6(b) which is consistent with Cyg X-1 has model parameters for radial infalling photons ( $E_{\text{ph}} = 3.5$  keV) from a thin disk [41], that either undergo PCS by equatorially confined orbiting target electrons ( $E_e \simeq 0.539$  MeV) or PPP ( $\gamma\gamma \rightarrow e^-e^+$ ) at  $r_{\text{mb}}$  or  $r_{\text{ph}}$ , respectively: the blueshifted energies (due to frame dragging) attained by the  $\sim 80\%$  up to  $95\%$  escaping particles, returning to the disk to be reprocessed and/or escaping to infinity, are the following: for the PCS photons,  $E'_{\text{ph}} \sim 11 - 250$  keV (i.e., up to  $\sim 70 E_{\text{ph}}$ ), with relative incoming and outgoing photon luminosities  $(L_\gamma)_{\text{out}} \sim 0.2 - 70 (L_\gamma)_{\text{in}}$ , respectively; and for the relativistic PPP electrons (with  $E_{\gamma 2} \sim 6$  MeV),  $E_{\mp} \sim 4$  MeV [consistent with synchrotron radiation in the radio regime for  $B \sim 10^2$  gauss, and inverse Compton scattering (of disk photons) into the hard x-rays/soft  $\gamma$ -ray regime—with relative incoming and outgoing photon luminosities  $(L_\gamma)_{\text{out}} \sim 5 - 600 (L_\gamma)_{\text{in}}$ , for  $M \sim 30M_\odot$ , at  $\sim 200$  keV–4 MeV, respectively]—[cf. also Figs. 8(a) and 9(a)]; see [5,25,34,40,42] for details. The case similar to those of Figs. 3(a), 6(a), 7(a)-7(c) which is consistent with MCG—6-30-15 has model parameters for radial infalling photons ( $E_{\text{ph}} = 0.511$  keV) from a thin disk, that either undergo PCS by equatorially or nonequatorially confined orbiting target electrons ( $E_e \simeq 0.539$  MeV or  $E_e \simeq 0.918$  MeV, respectively) at  $r_{\text{mb}}$  or PPP ( $\gamma\gamma \rightarrow e^-e^+$ ) at  $r_{\text{ph}}$ : the blueshifted energies (due to frame dragging) attained by the  $\sim 66\%$  up to  $95\%$  escaping particles, returning to the disk to be reprocessed and/or escaping to infinity, are the following: for PCS photons,  $E'_{\text{ph}} \sim 3 - 54$  keV or  $E'_{\text{ph}} \sim 6 - 150$  keV for equatorially or nonequatorially confined orbiting target electrons, respectively, with relative photon luminosities  $(L_\gamma)_{\text{out}} \sim 0.3 - 30 (L_\gamma)_{\text{in}}$  or  $(L_\gamma)_{\text{out}} \sim 0.5 - 135 (L_\gamma)_{\text{in}}$ , respectively; and for the relativistic PPP electrons (with  $E_{\gamma 2} \simeq 3.4$  MeV),  $E_{\mp} \sim 2$  MeV [consistent with synchrotron radiation in the radio regime for  $B \sim 10^2$  gauss, and inverse Compton scattering (of disk photons) into the hard x-ray/soft  $\gamma$ -ray regime—with relative incoming and outgoing photon luminosities  $(L_\gamma)_{\text{out}} \sim 0.2 - 3 (L_\gamma)_{\text{in}}$ , for  $M \sim 10^8 M_\odot$ , at  $\sim 250$  keV – 1.5 MeV, respectively], suggesting relatively weak, less powerful and less prominent radio jets, i.e., a radio quiet AGN, like a Seyfert galaxy; see [5,25,34] for details. Thus, the consistency of the results of these Penrose process analyses with observations strongly suggests that the appropriate way to exact energy from a KBH is by the “Penrose-Williams” mechanism, described here and in [5,25,34,40]: using gravity as the controlling force—to distinguish it from BZ-type models, which use electromagnetism as the controlling force.

Lastly, I want to conclude with the comment, that, the physics described in this paper and the associated paper of [5], can be applied to different types of high energy-momentum exchange scattering processes, i.e., processes that would be expected to occur in the “hot” ergosphere of a rotating black hole, the intention being to extract rotational energy-momentum. An immediate future investigation would be to perform the proton-proton nuclear scattering of neutral pions  $\pi^0$ , and their subsequent  $\pi^0 \rightarrow \gamma\gamma$  decay (see [5,8,20]), inside the ergosphere of a KBH. These  $\gamma$ -rays are presumed to be important in the population of the photon orbit in the highest energy PPP ( $\gamma\gamma \rightarrow e^-e^+$ ) processes. Note, similar nuclear scattering and  $\pi^0$ -decay processes, however, for particles confined to the equatorial plane are investigated in [3].

## ACKNOWLEDGMENTS

First, I thank God for His thoughts and for making this research possible. Next, I wish to thank Dr. Henry Kandrup for helpful comments and discussions, in particular those concerning the gravitomagnetic field, and for his careful reading of this manuscript. I am grateful to Drs. Fernando de Felice and Bernard Whiting for their comments and suggestions. Also, I thank Dr. Roger Penrose for his continual encouragement. Finally, I thank North Carolina A & T State University for their hospitality while this work was being completed. Part of this work was done at the

- [1] H. Thirring and J. Lense, *Phys. Z.* **19**, 156 (1918).
- [2] R. Penrose, *Rivista Del Nuovo Cimento: Numero Speciale* **1**, 252 (1969).
- [3] T. Piran and J. Shaham, *Phys. Rev. D.* **16**, No. 6, 1615 (1977).
- [4] T. Piran and J. Shaham, *Astrophys. J.* **214**, 268 (1977).
- [5] R. K. Williams, *Phys. Rev. D* **51**, 5387 (1995).
- [6] T. Piran, J. Shaham, and J. Katz, *Astrophys. J. Lett.* **196**, L107 (1975).
- [7] J. M. Bardeen, W. H. Press, and S. A. Teukolsky, *Astrophys. J.* **178**, 347 (1972).
- [8] J. A. Eilek and M. Kafatos, *Astrophys. J.* **271**, 804 (1983).
- [9] D. Leiter and M. Kafatos, *Astrophys. J.* **226**, 32 (1978); M. Kafatos and D. Leiter, *Astrophys. J.* **229**, 46 (1979).
- [10] K. S. Thorne, R. H. Price, and D. A. Macdonald, *Black Holes: The Membrane Paradigm* (Yale University Press, New Haven, 1986).
- [11] D. L. Jones, in *Superluminal Radio Sources*, edited by J. A. Zensus and T. J. Pearson (Cambridge University Press, Cambridge, 1987).
- [12] J. Dennett-Thorpe, A. H. Bridle, P. A. G. Scheuer, R. A. Laing, and J. P. Leahy, *Mon. Not. R. Astron. Soc.* **289**, 753 (1997).
- [13] I. F. Mirabel and L. F. Rodriguez, *Nature* **392**, 673 (1998).
- [14] R. M. Hjellming and M. P. Ruben, *Nature* **375**, 464 (1995).
- [15] R. P. Kerr, *Phys. Rev. Letters* **11**, 237 (1963).
- [16] R. H. Boyer and R. W. Lindquist, *J. Math. Phys.* **8**, 265 (1967).
- [17] K. S. Thorne, *Astrophys. J.* **191**, 507 (1974).
- [18] B. Carter, *Phys. Rev.* **174**, No. 5, 1559 (1968).
- [19] D. C. Wilkins, *Phys. Rev. D* **5**, 814 (1972).
- [20] J. A. Eilek, *Astrophys. J.* **236**, 664 (1980).
- [21] S. L. Shapiro, A. P. Lightman, and D. M. Eardley, *Astrophys. J.* **204**, 187 (1976).
- [22] A. P. Lightman, *Astrophys. J.* **194**, 429 (1974).
- [23] R. Mahadevan, R. Narayan, and J. Krolik, *Astrophys. J.* **486**, 268 (1997).
- [24] J. A. Eilek (private communication).
- [25] R. K. Williams, submitted to *Astrophys. J.* (1999).
- [26] F. de Felice and O. Zanotti, *Gen. Relativ. Gravit.* **32**, 1449 (2000); F. de Felice and L. Carlotto, *Astrophys. J.* **481**, 116 (1997).
- [27] R. D. Blandford, C. F. McKee, and M. J. Rees, *Nature* **267**, 211 (1977).
- [28] R. D. Blandford and A. Königl, *Astrophys. J.* **232**, 34 (1979).
- [29] C. D. Dermer, R. Schlickeiser, and A. Mastichiadis, *Astron. Astrophys.* **256**, L27 (1992).
- [30] L. Maraschi, G. Ghisellini, G., and A. Celotti, *Astrophys. J. Lett.* **397**, L5 (1992).
- [31] P. D. Barthel, in *Superluminal Radio Sources*, edited by J. A. Zensus and T. J. Pearson (Cambridge University Press, Cambridge, 1987).
- [32] A. H. Bridle and R. A. Perley, *Ann. Rev. Astr. Ap.* **22**, 319 (1984).
- [33] P. Parma, C. Fanti, R. Morganti, and H. R. de Ruiter, *Astron. Astrophys.* **181**, 244 (1987).
- [34] R. K. Williams, in *Relativistic Astrophysics: 20th Texas Symposium*, edited by J. C. Wheeler and H. Martel (American Institute of Physics, New York, 2001), astro-ph/0111161.
- [35] J. Wilms *etal.*, *Mon. Not. R. Astron. Soc.* (in press), astro-ph/0110520.
- [36] B. Punnsly and F. V. Coroniti, *Phys. Rev. D*, **40**, 3834 (1989); *Astrophys. J.* **350**, 518 (1990); **354**, 583 (1990); B. Punnsly, *Astrophys. J.* **372**, 424 (1991).
- [37] S. A. Balbus and J. F. Hawley, *Astrophys. J.* **376**, 214 (1991).
- [38] C. Cunningham, *Astrophys. J.* **208**, 334 (1976).
- [39] E. P. Liang, *Phys. Rep.* **302**, 67 (1998).
- [40] R. K. Williams and R. M. Hjellming (posthumous), to be submitted to *Astrophys. J.*, in preparation (2002).
- [41] I. D. Novikov and K. S. Thorne, in *Black Holes*, edited by C. DeWitt and B. S. DeWitt (Gordon and Breach, New York, 1973).
- [42] R. K. Williams, Ph.D. thesis, Indiana University, 1991.

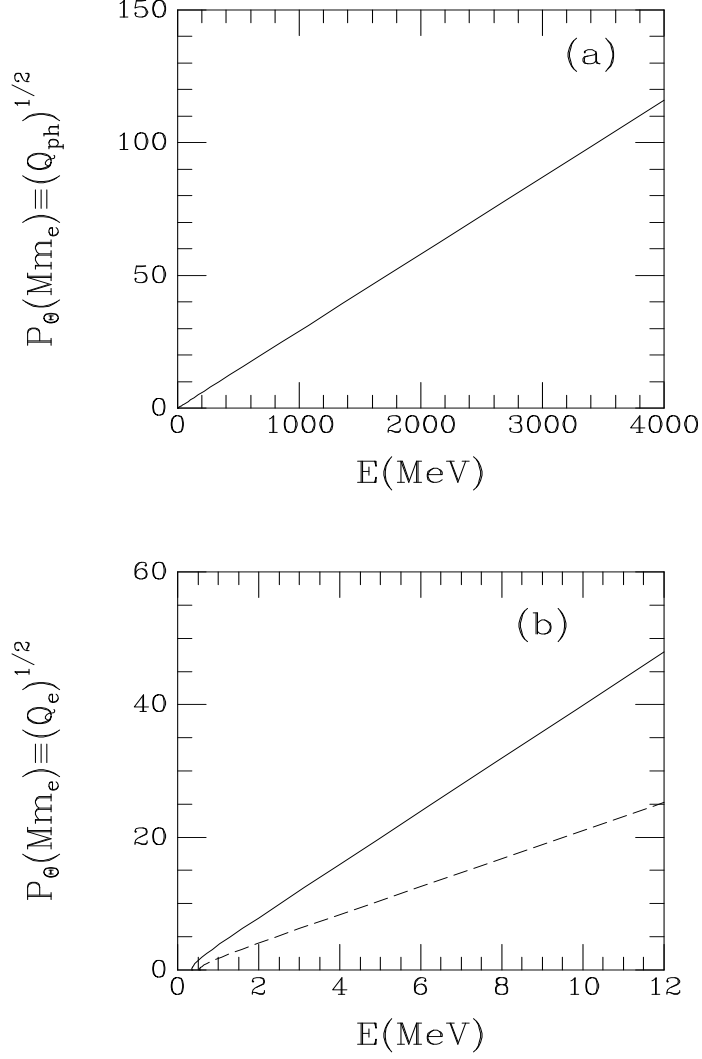


FIG. 1. Orbital parameters of massless and material particles. Magnitude of polar coordinate angular momentum  $P_\theta$  as the bound orbit crosses the equatorial plane ( $\equiv Q^{1/2}$ ) vs. the conserved nonequatorially confined orbital energy: (a)  $(P_{\text{ph}})_\theta$  vs.  $E_{\text{ph}}$  at the photon orbit,  $r_{\text{ph}} \simeq 1.074M$ . (b)  $(P_e)_\theta$  vs.  $E_e$ , of an orbiting electron, at  $r_{\text{mb}} \simeq 1.089M$  (dashed curve) and at  $r_{\text{ms}} \simeq 1.2M$  (solid curve). Notice that, as these momenta go to zero, each of the orbital energies goes to its equatorial confinement value—i.e., as  $Q_{\text{ph}}^{1/2} \rightarrow 0$ ,  $E_{\text{ph}} \rightarrow 0$ ; as  $Q_e^{1/2} \rightarrow 0$ ,  $E_e \rightarrow 0.539$  MeV at  $r_{\text{mb}}$ , and  $E_e \rightarrow 0.349$  MeV at  $r_{\text{ms}}$ . (Note that, when the more exact value of  $r_{\text{mb}} = 1.091M$  is used,  $E_e \rightarrow 0.512$  MeV  $\simeq \mu_e$ .)

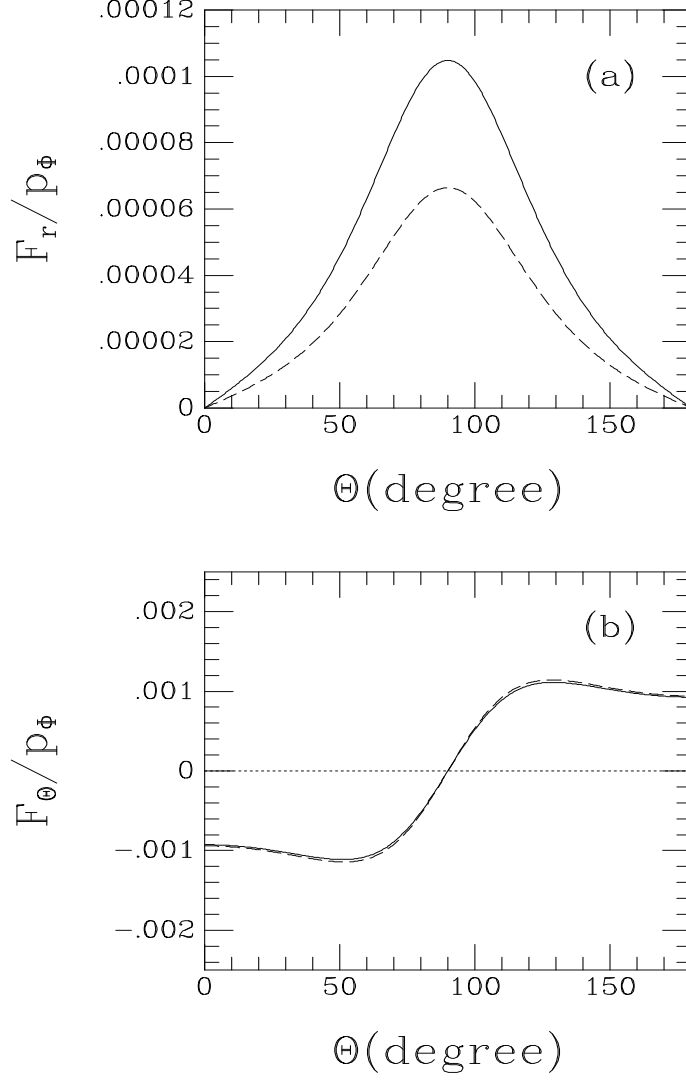


FIG. 2. The GM field force components. (a) The radial component:  $(f_{GM})_r/p_\Phi$  vs.  $\Theta$ . (b) The polar coordinate component:  $(f_{GM})_\Theta/p_\Phi$  vs.  $\Theta$ . The solid curves indicate the force at  $r_{mb} \simeq 1.089M$ ; the dashed curves indicate the force at  $r_{ph} \simeq 1.074M$ .

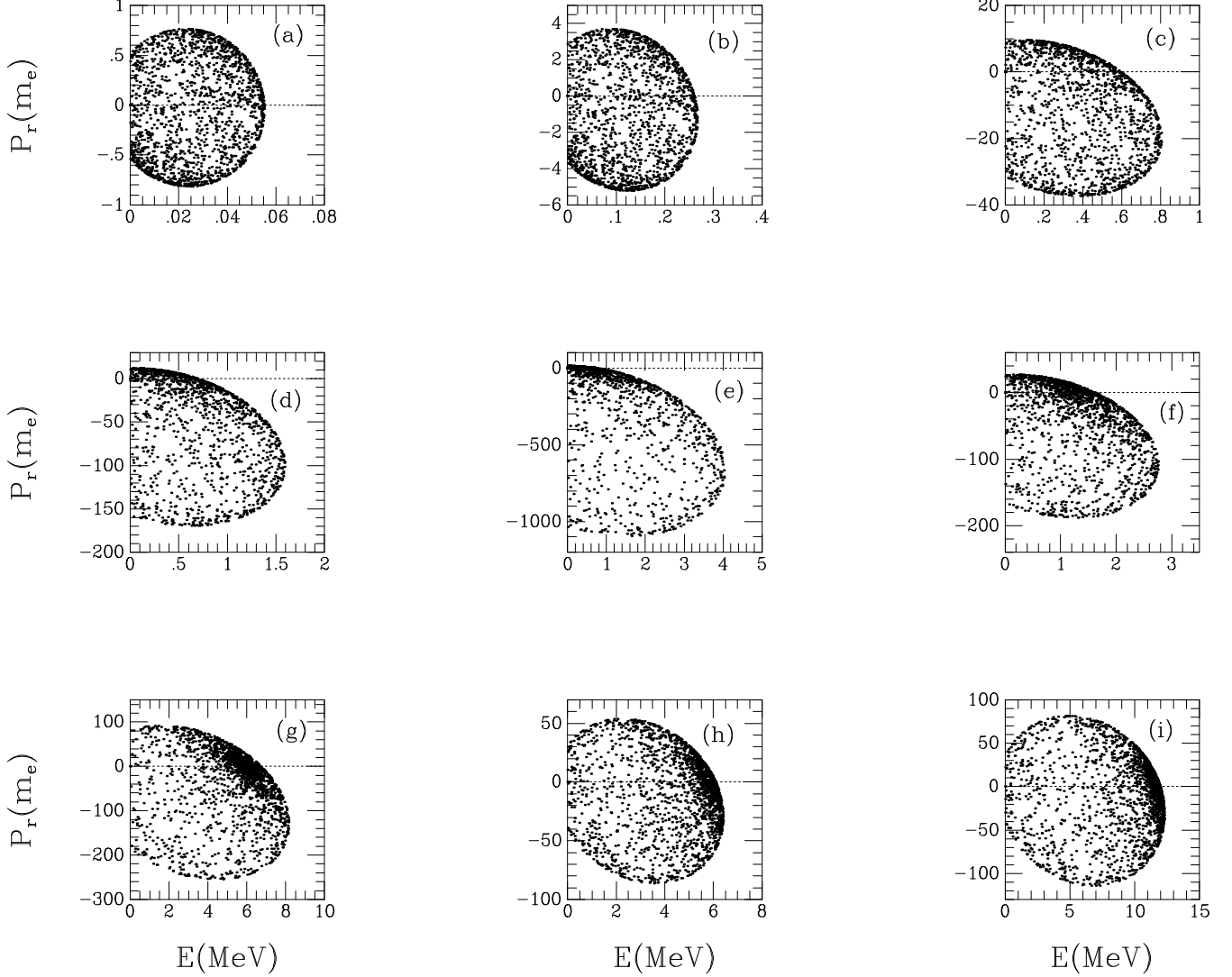


FIG. 3. Compton scattering: scatter plots showing radial momentum components:  $(P'_{\text{ph}})_r$  vs.  $E'_{\text{ph}}$ , of scattered escaping photons after 2000 events (each point represents a scattering event), at  $r_{\text{mb}} \simeq 1.089M$ . The various cases are defined by the following parameters:  $E_{\text{ph}}$ , initial photon energy;  $E_e$ , target electron orbital energy;  $Q_e^{1/2}$ , corresponding polar coordinate momentum  $(P_e)_\Theta$  of the target electron;  $N_{\text{es}}$ , number of photons escaping. (a)  $E_{\text{ph}} = 0.511$  keV,  $E_e = 0.539$  MeV,  $Q_e^{1/2} = 0$ ,  $N_{\text{es}} = 1707$ . (b)  $E_{\text{ph}} = 3.5$  keV,  $E_e = 0.539$  MeV,  $Q_e^{1/2} = 0$ ,  $N_{\text{es}} = 1637$ . (c)  $E_{\text{ph}} = 0.03$  MeV,  $E_e = 0.539$  MeV,  $Q_e^{1/2} = 0$ ,  $N_{\text{es}} = 1521$ . (d)  $E_{\text{ph}} = 0.15$  MeV,  $E_e = 0.539$  MeV,  $Q_e^{1/2} = 0$ ,  $N_{\text{es}} = 1442$ . (e)  $E_{\text{ph}} = 1$  MeV,  $E_e = 0.539$  MeV,  $Q_e^{1/2} = 0$ ,  $N_{\text{es}} = 1390$ . (f)  $E_{\text{ph}} = 0.15$  MeV,  $E_e = 1.297$  MeV,  $Q_e^{1/2} = \pm 2.479 Mm_e$ ,  $N_{\text{es}} = 1628$ . (g)  $E_{\text{ph}} = 0.15$  MeV,  $E_e = 5.927$  MeV,  $Q_e^{1/2} = \pm 12.43 Mm_e$ ,  $N_{\text{es}} = 1843$ . (h)  $E_{\text{ph}} = 0.03$  MeV,  $E_e = 5.927$  MeV,  $Q_e^{1/2} = \pm 12.43 Mm_e$ ,  $N_{\text{es}} = 1935$ . (i)  $E_{\text{ph}} = 0.03$  MeV,  $E_e = 11.79$  MeV,  $Q_e^{1/2} = \pm 24.79 Mm_e$ ,  $N_{\text{es}} = 1971$ . (Note, due to a minor oversight leading to improper treatment in the computer simulation of the arccosine term in eq. (3.39) of [5], correct Fig. 3(i) presented here replaces Fig. 4(a) of [5].)

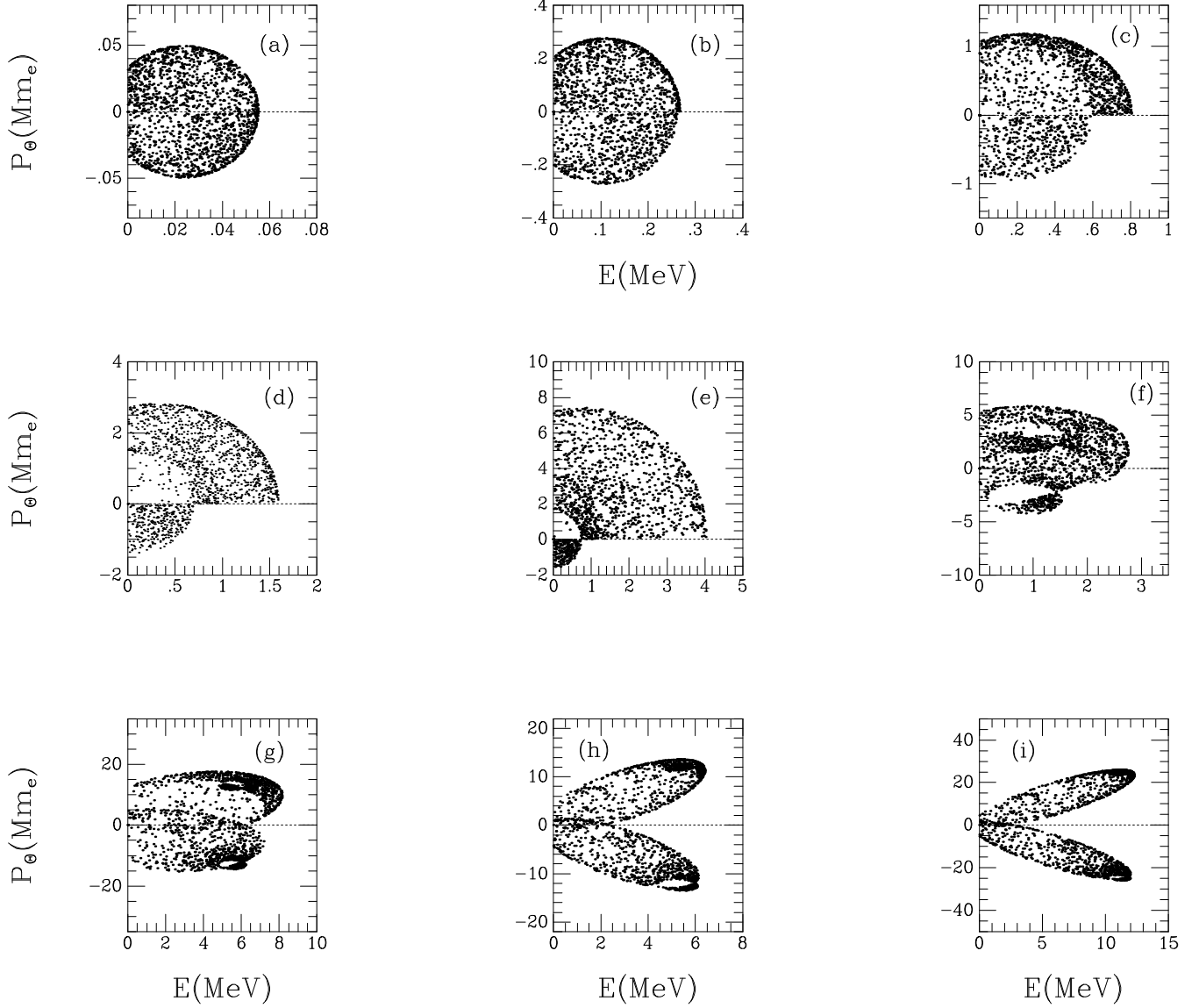


FIG. 4. Compton scattering: scatter plots showing the corresponding polar coordinate space momentum components:  $(P'_{\text{ph}})_{\Theta} [\equiv (Q'_{\text{ph}})^{1/2}]$  vs.  $E'_{\text{ph}}$ , of the escaping PCS photons, for the cases (a)–(i), respectively, described in Fig. 3. The units of  $(P'_{\text{ph}})_{\Theta}$  are  $Mm_e$  ( $G = c = 1$ ). (Note, due to a minor oversight leading to improper treatment in the computer simulation of the arccosine term in eq. (3.39) of [5], correct Figs. 4(b) and 4(c) presented here replace Figs. 7(a) and 3(c), respectively, of [5].)

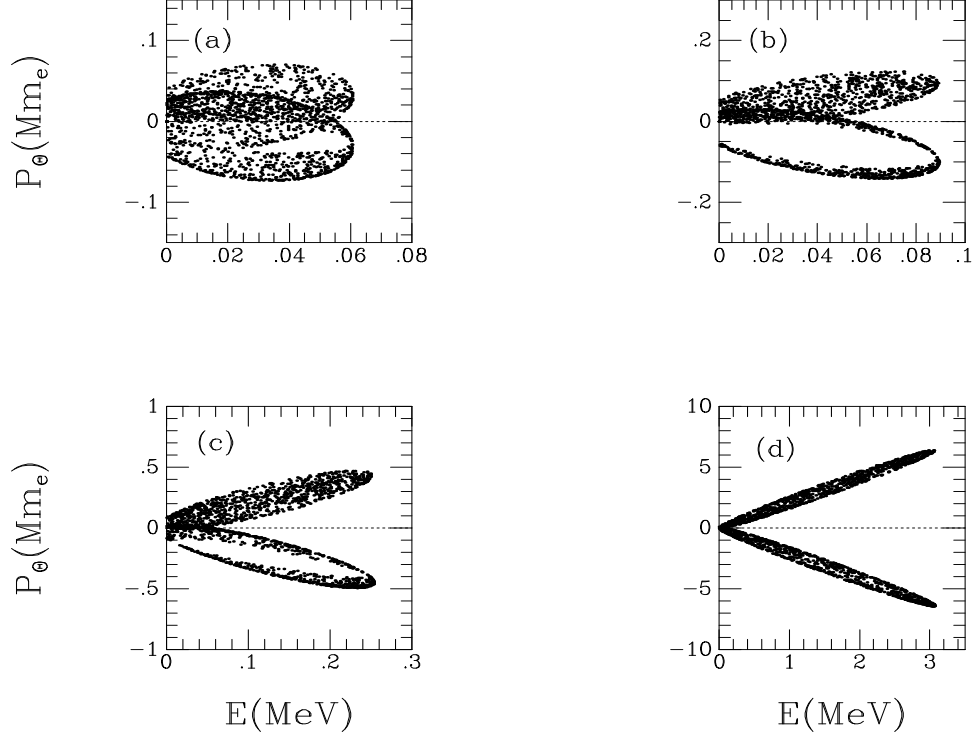


FIG. 5. Compton scattering: scatter plots showing polar coordinate space momentum components:  $(P'_{\text{ph}})_\Theta [\equiv (Q'_{\text{ph}})^{1/2}]$  vs.  $E'_{\text{ph}}$ , of the escaping PCS photons after 2000 events (each point represents a scattering event), at  $r_{\text{mb}} \simeq 1.089M$ . The various cases are defined by the following parameters:  $E_{\text{ph}}$ , initial photon energy;  $E_e$ , target electron orbital energy;  $Q_e^{1/2}$ , corresponding polar coordinate momentum  $(P_e)_\Theta$  of the target electron;  $N_{\text{es}}$ , number of photons escaping. (a)  $E_{\text{ph}} = 0.511$  keV,  $E_e = 0.570$  MeV,  $Q_e^{1/2} = \pm 0.393 Mm_e$ ,  $N_{\text{es}} = 1719$ . (b)  $E_{\text{ph}} = 0.511$  keV,  $E_e = 0.714$  MeV,  $Q_e^{1/2} = \pm 0.987 Mm_e$ ,  $N_{\text{es}} = 1779$ . (c)  $E_{\text{ph}} = 0.511$  keV,  $E_e = 1.297$  MeV,  $Q_e^{1/2} = \pm 2.479 Mm_e$ ,  $N_{\text{es}} = 1896$ . (d)  $E_{\text{ph}} = 0.511$  keV,  $E_e = 5.927$  MeV,  $Q_e^{1/2} = \pm 12.43 Mm_e$ ,  $N_{\text{es}} = 1996$ .

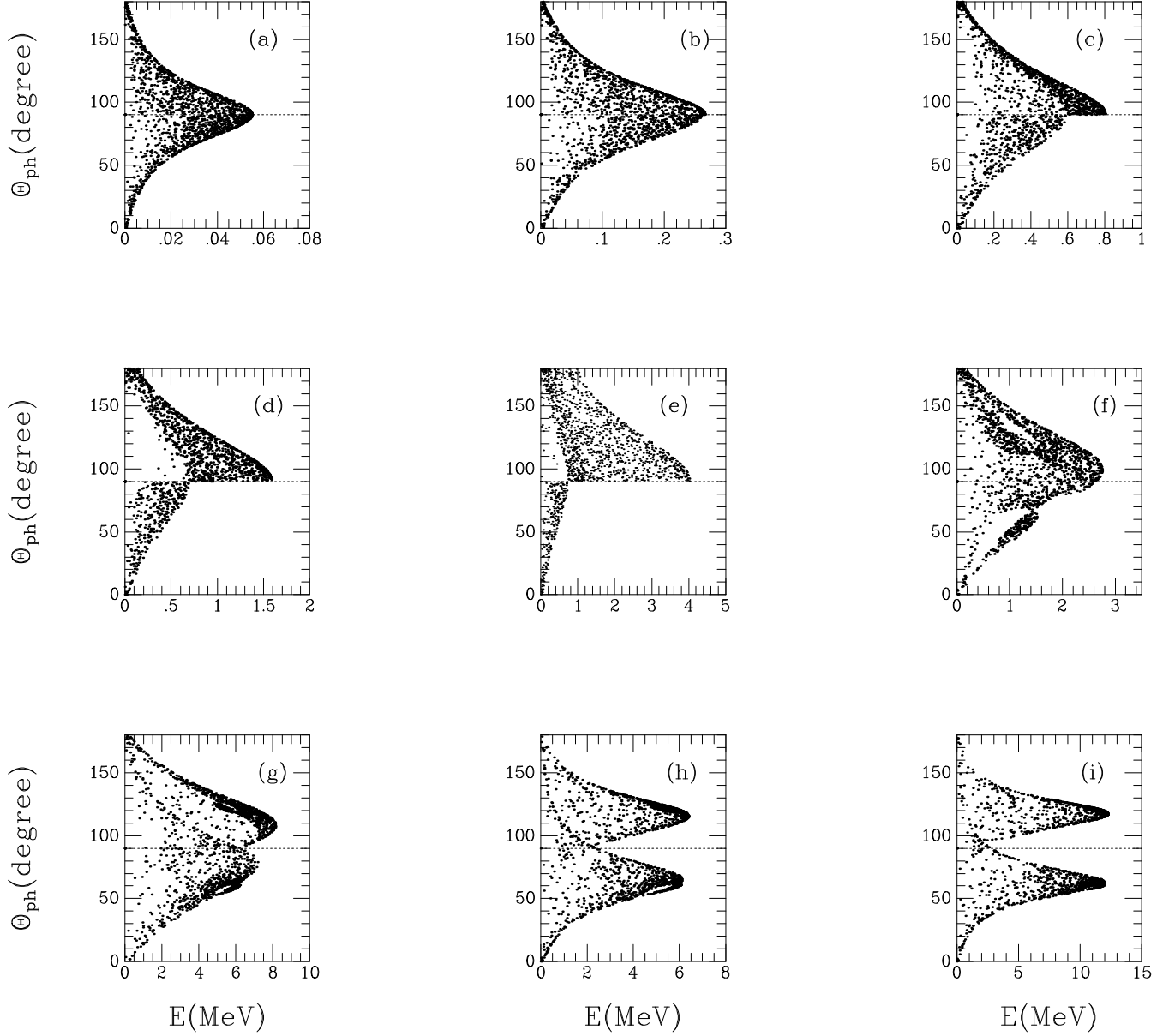


FIG. 6. Compton scattering: scatter plots displaying polar angles, above and below the equatorial plane:  $\Theta'_{\text{ph}}$  vs.  $E'_{\text{ph}}$ , of the escaping PCS photons, for the cases (a)–(i), respectively, described in Figs. 3 and 4. Note that,  $\Theta_{\text{ph}} > \pi/2$  is below the equatorial plane.

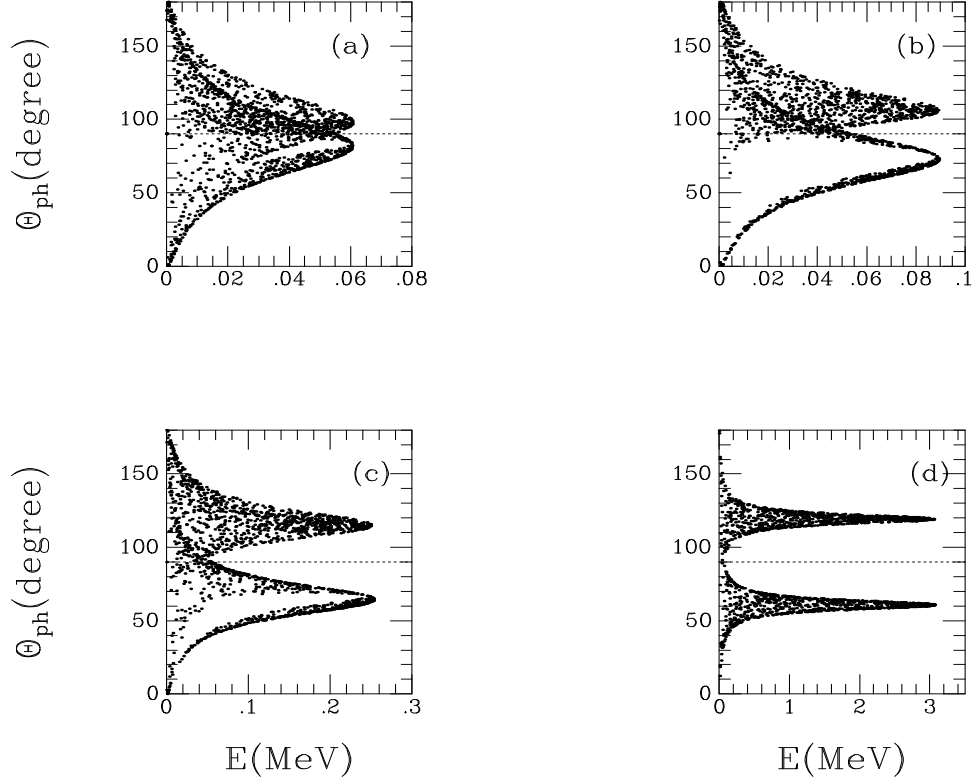


FIG. 7. Compton scattering: scatter plots displaying polar angles, above and below the equatorial plane:  $\Theta'_{\text{ph}}$  vs.  $E'_{\text{ph}}$ , of the escaping PCS photons, for the cases (a)–(d), respectively, described in Fig. 5. Note that,  $\Theta'_{\text{ph}} > \pi/2$  is below the equatorial plane.

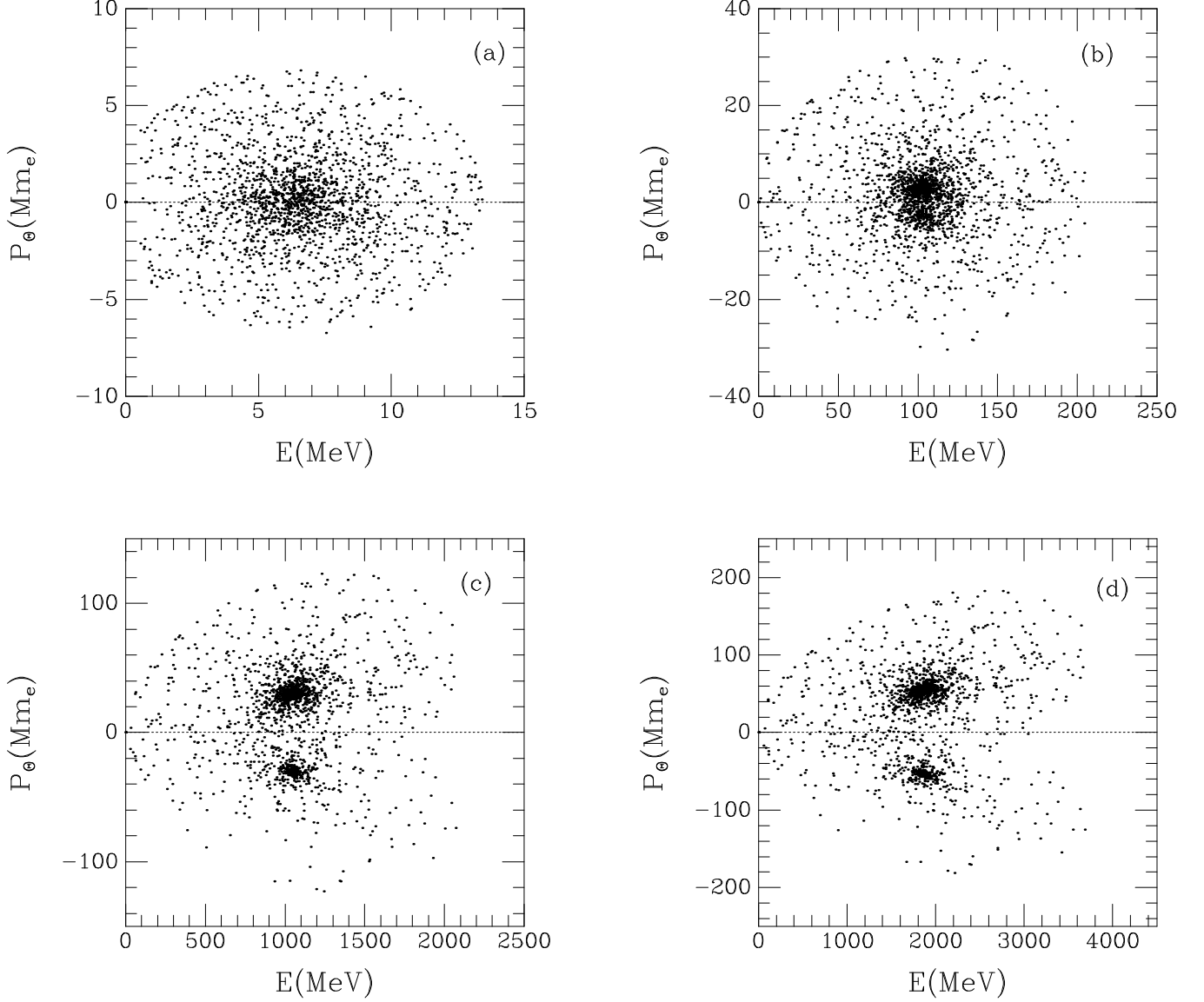


FIG. 8. Penrose pair production ( $\gamma\gamma \rightarrow e^-e^+$ ): scatter plots showing polar coordinate space momentum components:  $P_\Theta$  ( $\equiv Q^{1/2}$ ) vs.  $E_{\mp}$ , of scattered escaping  $e^-e^+$  pairs after 2000 events (each point represents a scattering event), at  $r_{\text{ph}}$ . The various cases are defined by the following parameters:  $E_{\gamma 1}$ , the infalling photon energy;  $E_{\gamma 2}$ , the target photon orbital energy;  $Q_{\gamma 2}^{1/2}$ , corresponding polar coordinate momentum  $(P_{\gamma 2})_\Theta$  of the target photon;  $N_{\text{es}}$ , number of  $e^-e^+$  pairs escaping. (a)  $E_{\gamma 1} = 0.03$  MeV,  $E_{\gamma 2} = 13.54$  MeV,  $Q_{\gamma 2}^{1/2} = \pm 0.393 Mm_e$ ,  $N_{\text{es}} = 1850$ . (b)  $E_{\gamma 1} = 0.03$  MeV,  $E_{\gamma 2} = 206.7$  MeV,  $Q_{\gamma 2}^{1/2} = \pm 6.0 Mm_e$ ,  $N_{\text{es}} = 1984$ . (c)  $E_{\gamma 1} = 0.03$  MeV,  $E_{\gamma 2} = 2.146$  GeV,  $Q_{\gamma 2}^{1/2} = \pm 62.28 Mm_e$ ,  $N_{\text{es}} = 1997$ . (d)  $E_{\gamma 1} = 0.03$  MeV,  $E_{\gamma 2} = 3.893$  GeV,  $Q_{\gamma 2}^{1/2} = \mp 113.0 Mm_e$ ,  $N_{\text{es}} = 1997$ .

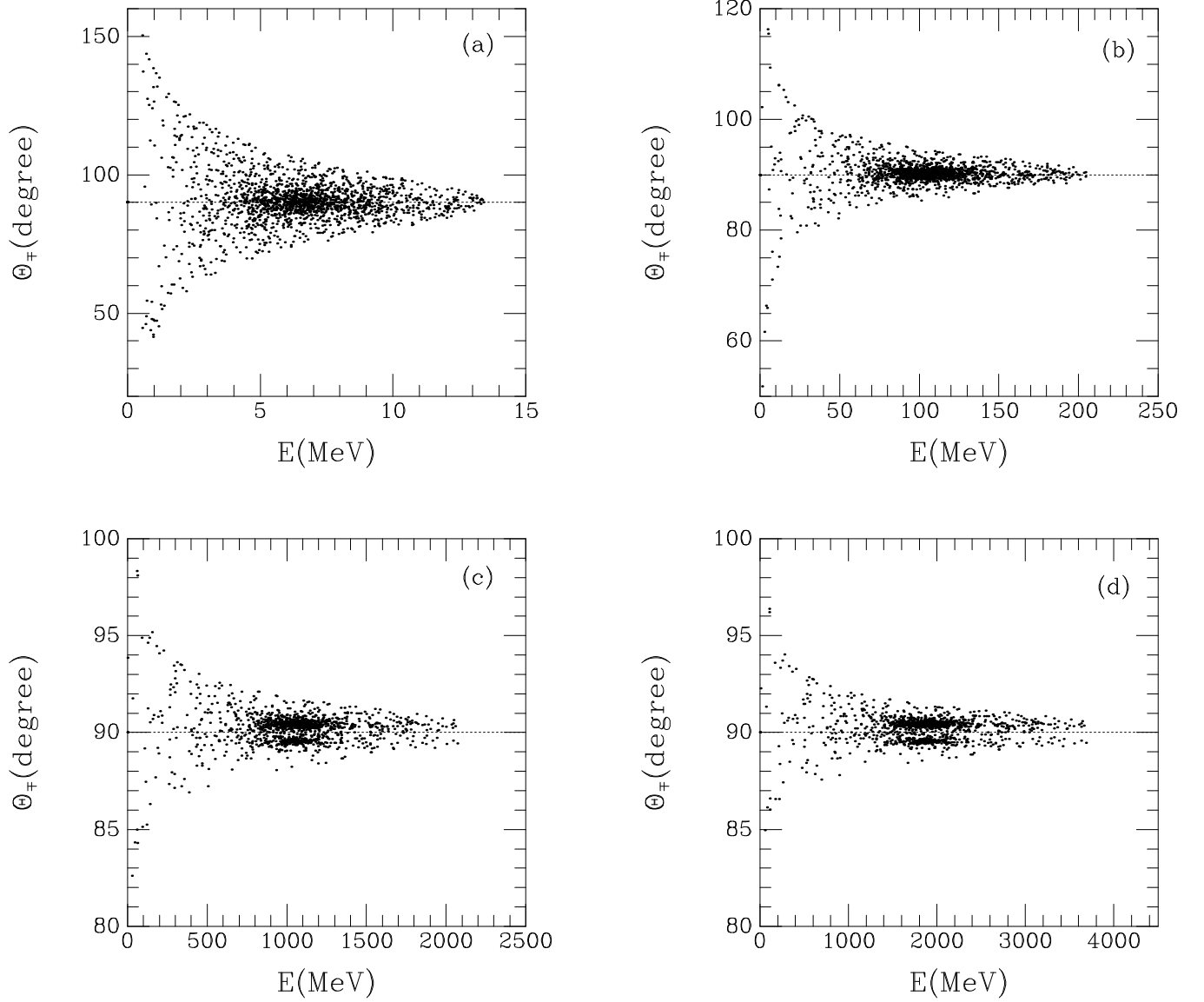


FIG. 9. Penrose pair production ( $\gamma\gamma \rightarrow e^-e^+$ ): scatter plots displaying polar angles, above and below the equatorial plane:  $\Theta_{\mp}$  vs.  $E'_{\mp}$ , of the escaping  $e^-e^+$  pairs, for the cases (a)–(d), respectively, described in Fig. 8.